

## Andromeda's Dust

B. T. Draine<sup>1,2</sup>, G. Aniano<sup>1,3</sup>, Oliver Krause<sup>4</sup>, Brent Groves<sup>4</sup>, Karin Sandstrom<sup>4</sup>, Robert Braun<sup>5</sup>, Adam Leroy<sup>6</sup>, Ulrich Klaas<sup>4</sup>, Hendrik Linz<sup>4</sup>, Hans-Walter Rix<sup>4</sup>, Eva Schinnerer<sup>4</sup>, Anika Schmiedeke<sup>4</sup>, and Fabian Walter<sup>4</sup>

### ABSTRACT

*Spitzer Space Telescope* and *Herschel Space Observatory* imaging of M31 is used, with a physical dust model, to construct maps of dust surface density, dust-to-gas ratio, starlight heating intensity, and polycyclic aromatic hydrocarbon (PAH) abundance, out to  $R \approx 25$  kpc. The global dust mass is  $M_d = 5.4 \times 10^7 M_\odot$ , the global dust/H mass ratio is  $M_d/M_H = 0.0081$ , and the global PAH abundance is  $\langle q_{\text{PAH}} \rangle = 0.039$ . The dust surface density has an inner ring at  $R = 5.6$  kpc, a maximum at  $R = 11.2$  kpc, and an outer ring at  $R \approx 15.1$  kpc. The dust/gas ratio varies from  $M_d/M_H \approx 0.026$  at the center to  $\sim 0.0027$  at  $R \approx 25$  kpc. From the dust/gas ratio, we estimate the interstellar medium (ISM) metallicity to vary by a factor  $\sim 10$ , from  $Z/Z_\odot \approx 3$  at  $R = 0$  to  $\sim 0.3$  at  $R = 25$  kpc. The dust heating rate parameter  $\langle U \rangle$  peaks at the center, with  $\langle U \rangle \approx 35$ , declining to  $\langle U \rangle \approx 0.25$  at  $R = 20$  kpc. Within the central kiloparsec, the starlight heating intensity inferred from the dust modeling is close to what is estimated from the stars in the bulge. The PAH abundance reaches a peak  $q_{\text{PAH}} \approx 0.045$  at  $R \approx 11.2$  kpc. When allowance is made for the different spectrum of the bulge stars,  $q_{\text{PAH}}$  for the dust in the central kiloparsec is similar to the overall value of  $q_{\text{PAH}}$  in the disk. The silicate–graphite–PAH dust model used here is generally able to reproduce the observed dust spectral energy distribution across M31, but overpredicts  $500\mu\text{m}$  emission at  $R \approx 2\text{--}6$  kpc, suggesting that at  $R = 2\text{--}6$  kpc, the dust opacity varies more steeply with frequency (with  $\beta \approx 2.3$  between  $200$  and  $600\mu\text{m}$ ) than in the model.

*Subject headings:* dust, extinction – infrared: galaxies – infrared: ISM

---

<sup>1</sup>Princeton University Observatory, Peyton Hall, Princeton, NJ 08544-1001, USA; draine@astro.princeton.edu

<sup>2</sup>Osservatorio Astrofisico Arcetri, Largo E. Fermi 5, I-50125 Firenze, Italy

<sup>3</sup>Institut d’Astrophysique Spatiale, F-91405 Orsay, France; ganiano@ias.u-psud.fr

<sup>4</sup>Max-Planck-Institut für Astronomie, Königstuhl 17, D-69117 Heidelberg, Germany

<sup>5</sup>CSIRO – Astronomy and Space Science, PO Box 76, Epping, NWS 1710, Australia

<sup>6</sup>National Radio Astronomy Observatory, 520 Edgemont Road, Charlottesville, VA 22903, USA

## 1. Introduction

The Andromeda galaxy, M31, is the nearest large spiral galaxy. At a distance  $D = 744 \text{ kpc}$ <sup>1</sup> (Vilardell et al. 2010), M31 provides an opportunity to study the dust and gas in an external star-forming galaxy with spatial resolution that is surpassed only for the Magellanic Clouds. The structure of the stellar spheroid, disk, and halo of M31 is the subject of ongoing investigations, now being carried out using photometry of large numbers of individual stars (e.g., Dalcanton et al. 2012).

The isophotal major radius is  $R_{25} = 95' = 20.6 \text{ kpc} @ 744 \text{ kpc}$  (de Vaucouleurs et al. 1991). M31 is classified as a SA(s)b spiral (de Vaucouleurs et al. 1991), but the gas and dust do not conform to a regular spiral pattern. Images of both H I (Braun et al. 2009; Chemin et al. 2009) and infrared emission (Haas et al. 1998; Barmby et al. 2006; Gordon et al. 2006; Fritz et al. 2012; Smith et al. 2012) show structure that appears as much ring-like as spiral in character. The centers of the rings are often offset significantly from the dynamical center of M31.<sup>2</sup> The off-center ring-like structure has been attributed to a nearly head-on collision with M32 (Block et al. 2006).

Previous studies of far-infrared (FIR) emission from the dust in M31 include maps made with *IRAS* (Habing et al. 1984; Devereux et al. 1994), *Infrared Space Observatory (ISO)* (Haas et al. 1998), and *Spitzer* (Gordon et al. 2006). The total infrared luminosity was well-measured, but the limited angular resolution of *IRAS* 60 and  $100 \mu\text{m}$  ( $105''$  FWHM), *ISO*  $175 \mu\text{m}$  ( $110''$  FWHM), and *Spitzer*  $160 \mu\text{m}$  ( $39''$  FWHM) allowed only a relatively coarse image of the dust distribution.

The present study takes advantage of the high sensitivity and angular resolution of *Herschel Space Observatory* (Pilbratt et al. 2010) to characterize the dust in M31 on angular scales as small as  $\sim 25''$  ( $= 90 \text{ pc} @ 744 \text{ kpc}$ ), and at wavelengths as long as  $500 \mu\text{m}$ , thereby capturing the emission from whatever cold dust may be present. The *Herschel* Exploitation of Local Galaxy Andromeda (HELGA; Fritz et al. 2012; Smith et al. 2012) recently employed *Herschel* imaging to study the dust distribution in M31, using single-temperature modified blackbody fits to the  $70 - 500 \mu\text{m}$  emission from each pixel. The present study differs from HELGA in two ways. First, we use an independent set of *Herschel* observations (Groves et al. 2012, O. Krause et al. 2013, in preparation), somewhat deeper than those obtained by HELGA. Secondly, we use a physical dust model (Draine & Li 2007) to model the spectral energy distribution (SED) from  $6 - 500 \mu\text{m}$ , and to estimate the dust mass surface density, intensities of starlight heating the dust, and the polycyclic aromatic hydrocarbon (PAH) abundance, using methods recently developed by Aniano et al. (2012) for studying the galaxies in the KINGFISH sample (Kennicutt et al. 2011).

The organization of the paper is as follows: the observational data are described in Section

---

<sup>1</sup>All radii, luminosities and masses in this paper have been corrected to  $D = 744 \text{ kpc}$ .

<sup>2</sup>For example, in model P1 of Corbelli et al. (2010) the center of the ring at 10–12 kpc is offset from the dynamical center by 0.6 kpc.

2, and the dust-model fitting methods are outlined in Section 3. Results are presented in Sections 4–8, where we estimate the total dust luminosity and mass, the dust/gas ratio, the metallicity as a function of radius, the characteristics of the starlight heating the dust, and the PAH abundance. Evidence for variation of the dust properties is discussed in Section 9. The results are summarized in Section 10.

Appendix A examines the inconsistency between PACS and MIPS photometry of M31. The starlight contribution from the M31 bulge stars is calculated in Appendix B.

## 2. Observational Data

M31 has been mapped using the IRAC (Fazio et al. 2004) and MIPS (Rieke et al. 2004) cameras on *Spitzer Space Telescope* (Werner et al. 2004). More recently, maps have been obtained by the PACS (Poglitsch et al. 2010) and SPIRE (Griffin et al. 2010) cameras on *Herschel* (Pilbratt et al. 2010).

The present analysis uses IRAC data from Barmby et al. (2006)<sup>3</sup> and MIPS data from Gordon et al. (2006).<sup>4</sup> The PACS and SPIRE imaging was done in parallel mode at medium scan speed ( $20'' \text{ s}^{-1}$ ) for a total time of  $\sim 24$  hr (O. Krause et al. 2013, in preparation), and are the same data as used by Groves et al. (2012), except for small changes in calibration. We use the most recent calibrations of PACS and SPIRE.<sup>5</sup> We refer to the different images by the camera name and nominal wavelength in microns: IRAC3.6, IRAC4.5, IRAC5.8, IRAC8.0, MIPS24, MIPS70, MIPS160, PACS70, PACS100, PACS160, SPIRE250, SPIRE350, and SPIRE500.

The center of M31 is located at  $\alpha_{\text{J2000}} = 10.685^\circ$ ,  $\delta_{\text{J2000}} = 41.269^\circ$  (Crane et al. 1992), or Galactic coordinates  $\ell = 121^\circ$ ,  $b = -22^\circ$ . Because M31 is only  $22^\circ$  from the Galactic plane, removal of the Galactic foreground “cirrus” emission is challenging, particularly in view of the large angular extent of M31. We are helped by the high inclination  $i \approx 78^\circ$  of M31, which raises the surface brightness, and increases the contrast with foreground and background emission.

Subtraction of foreground and background emission has been carried out following methods described in Aniano et al. (2012), with automatic identification of background pixels and fitting of a “tilted plane” background model (with three parameters – zero point, tilt, and tilt orientation) for

---

<sup>3</sup>IRAC images in bands 1–4 were multiplied by extended source calibration factors 0.91, 0.94, 0.66, 0.74 (Reach et al. 2005).

<sup>4</sup>MIPS images were generated by the Mips\_enhancer v3.10 pipeline on 2007 Jul 3.

<sup>5</sup> The PACS and SPIRE images were processed by HIPE v9, and the Level 1 HIPE images were then processed by Scanamorphos v18.0 (Roussel 2013). We used the calibration files in HIPE v9 (version 42 for PACS, and version 10.0 for SPIRE). Intensities in the SPIRE bands were obtained by dividing the HIPE v9 flux density per beam by effective beam solid angles  $\Omega = (1.103, 1.944, 4.183) \times 10^{-8}$  sr for SPIRE250, 350, and 500, as recommended by Griffin et al. (2013).

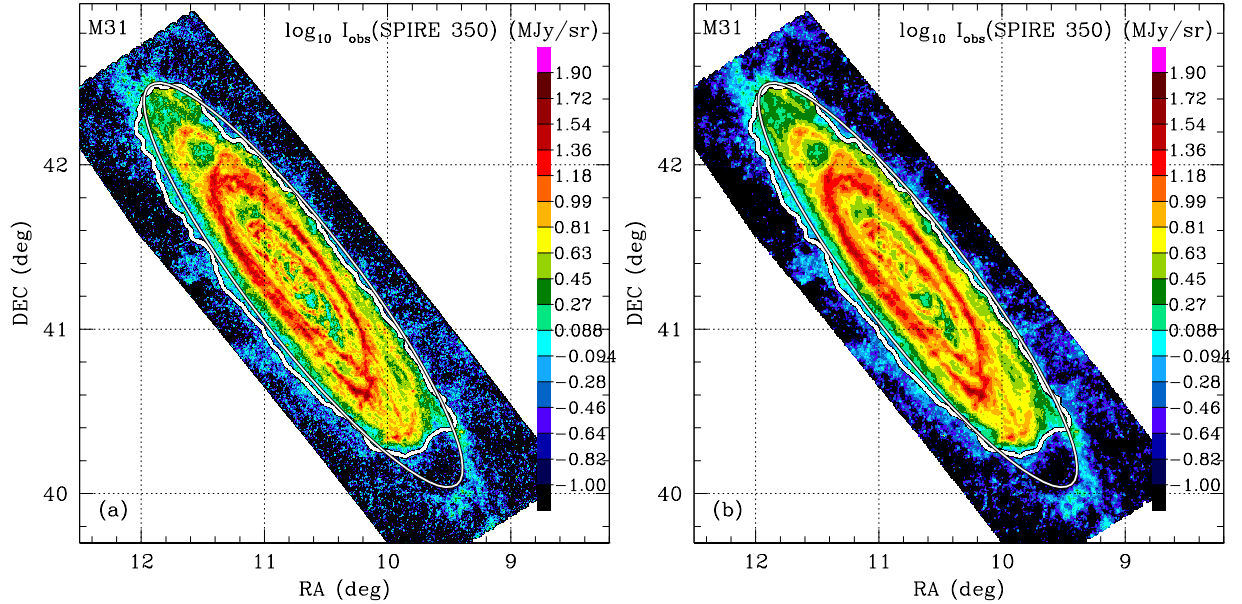


Fig. 1.— Background-subtracted  $350\mu\text{m}$  images of M31. Left: native resolution of SPIRE350. Right: SPIRE350 image convolved to the MIPS160 PSF. It is seen that most of the structure visible at S350 resolution remains at M160 resolution, with improved signal/noise in low surface brightness regions. The contour delineates the “galaxy mask”: the region within which the signal-to-noise ratio (S/N) is high enough that dust modeling can be done pixel-by-pixel (see text). The ellipse shown is a tilted circle of radius  $R = 5500'' = 19.8\text{ kpc} @ 744\text{ kpc}$  centered on the dynamical center, with inclination  $i = 77.7^\circ$  and P.A. =  $37.7^\circ$  (Corbelli et al. 2010).

all bands except IRAC5.8 and IRAC8.0. For IRAC5.8 and IRAC8.0, it was found that the simple “tilted plane” background model left obvious large-scale residuals, presumably a consequence of the large angular extent of M31. For IRAC5.8 and IRAC8.0, it was found necessary to use more complex curved surfaces, rather than simple tilted planes, to model the background. Even so, the background estimation for IRAC5.8 and IRAC8.0 seems to be less successful than for other bands, for reasons that are further discussed in Section 8.

The foreground cirrus has significant structure on  $\sim 1^\circ$  scales (see, e.g., the *IRAS*  $100\mu\text{m}$  or LAB 21 cm map of the area around M31), and the simple tilted plane model (or low-order curved surface in the case of IRAC5.8 and IRAC8.0) will not remove all of the foreground cirrus. This will be problematic in the low surface brightness outer regions of M31. However, after the foreground- and background-subtracted FIR images have been fitted by dust models, comparison of the resulting dust map with maps of the H I at the radial velocity of M31 will allow us to assess the effects of imperfect foreground subtraction. Except for IRAC5.8 and IRAC8.0, the present tilted plane foreground model appears adequate for  $R \lesssim 25\text{ kpc}$  (see Section 5).

For modeling the dust in resolved systems, it is essential that multiband imaging be convolved to a common point spread function (PSF). The present study is carried out at two angular resolutions: that of the SPIRE350 camera (FWHM= $24.9'' = 90\text{ pc} @ 744\text{ kpc}$ , henceforth referred to

as *S350 resolution*) and that of the MIPS160 camera (FWHM=39'' = 141 pc @ 744 kpc, henceforth referred to as *M160 resolution*). Image convolutions were carried out using kernels obtained as described by Aniano et al. (2011). For studies at S350 resolution, we are unable to use SPIRE500 or MIPS160 imaging, because the PSF of those cameras is too broad. The convolved images at S350 resolution were sampled with 10'' × 10'' pixels. Images convolved to M160 resolution were sampled with 18'' × 18'' pixels.

Figure 1 shows SPIRE350 images of M31; the left image is at S350 resolution; the image on the right is convolved to M160 resolution. The lower resolution of M160 is evident when the images are compared, but most details of the image that are seen at S350 resolution are also identifiable at M160 resolution. Analysis of M31 at M160 resolution – benefiting from the improved signal/noise of the larger M160 pixels as well as being able to use both SPIRE500 and MIPS160 data to constrain the models – will, therefore, not lose important structural features.

M31 is highly inclined. Using DRAO H I 21cm data, Chemin et al. (2009) estimated an average inclination  $i = 74.3^\circ$  and P.A. =  $37.7^\circ$  for the disk at  $R = 6 - 27$  kpc. From WSRT H I 21cm observations, Corbelli et al. (2010) obtain an inclination  $i = 77.7^\circ$  and position angle P.A. =  $37.7^\circ$  for  $R = 10 - 13$  kpc. Corbelli et al. (2010) showed that the H I kinematics can be described using circular rings with centers offset from the dynamical center of M31, and with inclinations between  $75^\circ$  and  $79^\circ$  for  $10 < R < 25$  kpc).

We will assume the disk to have a single inclination  $i = 77.7^\circ$  and position angle P.A. =  $37.7^\circ$ . Figure 1 shows ellipses with major radius 5500'' corresponding to  $R = 19.8$  kpc at  $D = 744$  kpc, with  $i = 77.7^\circ$  and P.A. =  $37.7^\circ$ . Radial trends will be studied by averaging in annuli centered on the location of the presumed supermassive black hole,  $\alpha_{J2000} = 10.6847^\circ$ ,  $\delta_{J2000} = 41.2690^\circ$  (Crane et al. 1992).

The S350 PSF provides excellent spatial resolution (FWHM = 90 pc along the major axis). We will compare results obtained at S350 resolution with results obtained using the M160 PSF. While the dust models at M160 resolution smooth out dust structures smaller than  $\sim 140$  pc along the major axis (or  $\sim 700$  pc along the minor axis), working at M160 resolution permits (1) extending the wavelength coverage to  $500\mu\text{m}$  (by including SPIRE500 photometry), and (2) using MIPS160 photometry, which is somewhat deeper than the PACS160 imaging. In addition, the larger pixels provide improved signal/noise in low surface brightness regions. At S350 resolution, the models are constrained by photometry in 11 bands (4 IRAC, 2 MIPS, 3 PACS, 2 SPIRE). At M160 resolution, MIPS160 and SPIRE500 are added, giving a total of 13 photometric constraints for each pixel. Comparison of model results at S350 and M160 resolution will provide insight into the reliability of the method.

### 3. Modeling the Dust and Starlight Heating

#### 3.1. Dust Model

We model the dust in M31 using the dust models of Draine & Li (2007, hereafter DL07). The dust is assumed to be a mixture of carbonaceous grains and amorphous silicate grains with a size distribution that is consistent with studies of the wavelength-dependent extinction and infrared emission produced by dust in the diffuse interstellar medium (ISM) in the solar neighborhood (Weingartner & Draine 2001, hereafter WD01). We treat the PAH abundance as variable, proportional to the parameter  $q_{\text{PAH}}$ , where  $q_{\text{PAH}}$  is defined to be the fraction of the total dust mass that is contributed by PAHs containing fewer than  $10^3$  C atoms.

The optical properties of the dust mixture are based on an adopted grain size distribution, dielectric functions for the graphite and silicate materials, and adopted absorption cross sections per C atom for the PAHs. Heat capacities are also required to calculate the temperature distribution function for the smaller carbonaceous and silicate grains (Draine & Li 2001).

By fitting the dust model to the extinction curve per H in the solar neighborhood, the grain volume per H is constrained. We assume the size distribution for the local Milky Way dust with  $R_V = 3.1$  obtained by WD01, but with all grain abundances relative to H lowered by the factor 0.93 recommended by Draine (2003).

Table 1: Grain Mass per H in the Solar Neighborhood

Material	$V$ (cm <sup>3</sup> /H)	$M_d/M_H$	$M_d/M_H$
	DL07	DL07	Renormalized DL07
Amorphous silicate	$3.68 \times 10^{-27}$	0.00836 <sup>a</sup>	0.00682 <sup>b</sup>
Carbonaceous	$2.11 \times 10^{-27}$	0.00277 <sup>c</sup>	0.00226 <sup>d</sup>
Total	$5.79 \times 10^{-27}$	0.0111 <sup>a,c</sup>	0.00908 <sup>b,d</sup>
Observed toward $\zeta$ Oph			0.0091 <sup>e</sup>

<sup>a</sup> For  $\rho_{\text{sil}} = 3.8 \text{ g cm}^{-3}$ .  
<sup>b</sup> For  $\rho_{\text{sil}} = 3.1 \text{ g cm}^{-3}$ .  
<sup>c</sup> For  $\rho_{\text{carb.}} = 2.2 \text{ g cm}^{-3}$ .  
<sup>d</sup> For  $\rho_{\text{carb.}} = 1.8 \text{ g cm}^{-3}$ .  
<sup>e</sup> From Table 23.1 of Draine (2011b).

#### 3.2. Renormalization of the DL07 Dust Mass

The dust volume/H in the DL07 dust model is determined by fitting the observed extinction in the solar neighborhood; the dust mass/H can then be calculated if solid densities are assumed

Table 2: Some Properties of Renormalized DL07 Dust Model

Property	Silicates	Carbonaceous	<b>Total</b>
$A_V/\Sigma_{M_d}$ (mag/( $M_\odot$ pc $^{-2}$ ))	5.403	13.39	7.394
$\kappa(60\mu\text{m})$ (cm $^2$ g $^{-1}$ )	102.5	106.3	103.4
$\kappa(70\mu\text{m})$ (cm $^2$ g $^{-1}$ )	73.62	72.24	73.28
$\kappa(100\mu\text{m})$ (cm $^2$ g $^{-1}$ )	34.59	29.02	33.20
$\kappa(160\mu\text{m})$ (cm $^2$ g $^{-1}$ )	13.11	10.69	12.51
$\kappa(250\mu\text{m})$ (cm $^2$ g $^{-1}$ )	5.263	3.981	4.941
$\kappa(350\mu\text{m})$ (cm $^2$ g $^{-1}$ )	2.448	2.060	2.351
$\kappa(500\mu\text{m})$ (cm $^2$ g $^{-1}$ )	1.198	1.062	1.164
$\kappa(850\mu\text{m})$ (cm $^2$ g $^{-1}$ )	0.4865	0.4202	0.4699
$\kappa(1.28\text{ mm})$ (cm $^2$ g $^{-1}$ )	0.2224	0.1866	0.2135
$\kappa(2.10\text{ mm})$ (cm $^2$ g $^{-1}$ )	0.1130	0.0914	0.1076

$\kappa$  = absorption cross section per unit dust mass

for the dust materials. For the silicates, DL07 assumed a density  $\rho = 3.8\text{ g cm}^{-3}$ , and for the carbonaceous grains the density contributed by carbon alone was taken to be  $\rho_C = 2.2\text{ g cm}^{-3}$ . With these adopted densities, the DL07 dust model that reproduces the extinction per H in the solar neighborhood has  $M_d/M_H = 0.0112$  (see Table 1). The dust mass estimates in Aniano et al. (2012) are based on the original DL07 value  $M_d/M_H = 0.0112$  for dust in the solar neighborhood.

However, as noted by Draine et al. (2007), this dust mass/H is in mild conflict with elemental abundances in the solar-neighborhood ISM: the total mass of elements “depleted” from the gas in the diffuse ISM is estimated to be less than what would be calculated for the WD01 dust model with the above solid densities. For the well-studied sightline toward  $\zeta$  Oph, the observed depletions imply  $M_d/M_H = 0.0091 \pm 0.0006$  (Draine 2011b, Table 23.1).<sup>6</sup>

In the present paper we will assume solar neighborhood dust to have  $M_d/M_H = 0.0091$ . This can be reconciled with the volume of grain material required by the WD01 extinction model if the grain solid densities are reduced by a factor  $\sim 0.81$ . Here we define the “renormalized DL07” model to be the same grain size distributions (i.e., same volume of grain material) and same dielectric functions as used by DL07, but with the silicate density  $\rho_{\text{sil}}$  reduced from  $3.8\text{ g cm}^{-3}$  to  $3.1\text{ g cm}^{-3}$ , and the density of carbonaceous grain material reduced from  $2.1\text{ g cm}^{-3}$  to  $1.8\text{ g cm}^{-3}$ . Table 2 gives  $A_V/\Sigma_{M_d}$  for the renormalized DL07 model, as well as opacities at selected FIR wavelengths.

With this renormalization, all dust masses and dust/H ratios in Aniano et al. (2012) should

---

<sup>6</sup>This value involves an assumption about the oscillator strength for C II]2325Å and a second assumption about the depletion of oxygen – see Draine (2011b).

be reduced by a factor  $f_M = 0.00908/0.01113 = 0.816$ . In this renormalized model for dust in the diffuse ISM, 75.1% of the dust mass is provided by the amorphous silicates, and 24.9% by the carbonaceous component (PAHs included).

### 3.3. Dust Masses and Starlight Intensities

The present study seeks to estimate dust masses in M31 by modeling the observed FIR and submillimeter emission. The dust is assumed to be heated by starlight, and the modeling has the freedom to adjust the starlight intensities such that the grains are heated to temperatures such that their emission spectrum is consistent with the observed shape of the SED. Then, with the dust temperatures set by the starlight heating rates, the dust mass is proportional to the observed emission. Note that there is no single temperature characterizing the dust – even in a single radiation field, grains of different size and composition have different temperatures, and the very small grains undergo temperature fluctuations due to single-photon heating. Additionally, a single “pixel” – which may be several hundred parsecs in transverse dimension – may include subregions with different starlight intensities.

For a given starlight intensity  $U$ , grain size  $a$  and composition, we solve for the temperature probability distribution  $(dP/dT)_{U,a,\text{comp}}$ . For large grains  $dP/dT$  can be approximated by a  $\delta$ -function, but for small grains  $dP/dT$  can be very broad, and must be solved for as described by Li & Draine (2001). The time-averaged emission spectrum for a grain is then

$$(p_\nu)_{U,a,\text{comp}} = 4\pi \int dT (dP/dT)_{U,a,\text{comp}} (C_{\text{abs},\nu})_{a,\text{comp}} B_\nu(T) \quad , \quad (1)$$

where  $(C_{\text{abs},\nu})_{a,\text{comp}}$  is the absorption cross section at frequency  $\nu$ . The emission per unit mass for a dust mixture exposed to starlight  $U$  is

$$\left( \frac{dL_\nu}{dM_d} \right)_U = \frac{\sum_{\text{comp}} \int da (dn/da)_{\text{comp}} (p_\nu)_{U,a,\text{comp}}}{\sum_{\text{comp}} \int da (dn/da)_{\text{comp}} (4\pi/3)a^3 \rho_{\text{comp}}} \quad , \quad (2)$$

where  $\rho_{\text{comp}}$  is the solid density, and  $(dn/da)_{\text{comp}}$  is the size distribution. The luminosity of a region  $j$  is obtained by summing over the starlight distribution:

$$L_{\nu,j} = \int dU \frac{dM_{d,j}}{dU} \left( \frac{dL_\nu}{dM_d} \right)_U \quad . \quad (3)$$

For a region  $j$  of solid angle  $\Omega_j$ , with dust mass  $M_{d,j} = \Sigma_{M_{d,j}} \Omega_j D^2$ , the dust mass  $dM_{d,j}$  exposed to starlight intensities in  $[U, U + dU]$  is assumed to be given by the simple parameterization proposed by DL07:

$$\frac{dM_{d,j}}{dU} = \Sigma_{M_{d,j}} \Omega_j D^2 \left[ (1 - \gamma_j) \delta(U - U_{\text{min},j}) + \gamma_j \frac{(\alpha_j - 1) U^{-\alpha_j}}{U_{\text{min},j}^{1-\alpha_j} - U_{\text{max}}^{1-\alpha_j}} \right] \quad , \quad (4)$$

where  $\Sigma_{M_{d,j}}$  is the total dust mass surface density in region  $j$ ,  $\delta$  is the Dirac  $\delta$ -function, and  $\alpha_j > 1$  is a power-law index characterizing the distribution of starlight intensities. A fraction



$(1 - \gamma_j)$  of the dust mass is heated by starlight intensity  $U = U_{\min,j}$ , with the remaining fraction  $\gamma_j$  exposed to starlight with intensities  $U_{\min,j} < U \leq U_{\max}$ , with a power-law distribution  $dM_d/dU \propto U^{-\alpha_j}$ . For NGC 628 and NGC 6946, Aniano et al. (2012) found that the parameter  $U_{\max}$  could be fixed at  $U_{\max} = 10^7$  without significantly degrading the quality of the fits, hence we also fix  $U_{\max} = 10^7$ . Thus, for each region  $j$ , we have five adjustable parameters characterizing the dust:  $\{\Sigma_{M_d,j}, q_{\text{PAH},j}, U_{\min,j}, \alpha_j, \gamma_j\}$ .<sup>7</sup> We require  $\Sigma_{M_d,j} \geq 0$ ,  $0 \leq \gamma_j \leq 1$ , and  $1 < \alpha_j < 3$ . We use one additional parameter to characterize the contribution of direct starlight (taken to have the spectrum of a 5000K blackbody) to the photometry for pixel  $j$ . Thus each region has 6 adjustable parameters, and either 11 or 13 data, depending on whether we use S350 or M160 resolution. Because MIPS70 and PACS70 cover essentially the same wavelengths, and likewise for MIPS160 and PACS160, the effective number of constraints is 10 (at S350 resolution) or 11 (at M160 resolution).

The fitting procedure assumes the DL07 model dust to be heated by starlight with the solar-neighborhood spectrum found by Mathis et al. (1983). In Sections 7 and 8 we examine the effects of changes in the starlight spectrum when the bulge stars make a significant contribution to the dust heating.

### 3.4. Systematic Uncertainties in Dust Mass Estimation

The model SED depends on the modeled distribution of dust temperatures *and* on the wavelength-dependence of the dust opacity  $\kappa_\nu$ . The wavelength-dependence of  $\kappa_\nu$  is tested by whether the model can reproduce the observed shape of the SED, but if  $\kappa_\nu$  is in error by some constant factor  $A$ , the derived dust masses will be off by a factor  $1/A$ .

The DL07 dust model uses adopted dielectric functions for the amorphous silicate and carbonaceous grains which, with the assumption of spherical shape, allows absorption cross sections to be calculated. For solar-neighborhood abundances, the absorption cross section per H is given in Table 3 for  $\lambda = 100\mu\text{m}$ ,  $250\mu\text{m}$ , and  $500\mu\text{m}$ .

Planck Collaboration et al. (2011) examined the FIR emission in the diffuse ISM, finding that the SED for low-velocity H I was consistent with  $\kappa \propto \nu^\beta$ , with  $\beta \approx 1.8$ , and  $\tau(250\mu\text{m})/N_{\text{H}} = (1.0 \pm 0.3) \times 10^{-25} \text{ cm}^2/\text{H}$ . As seen in Table 3, the *Planck* estimate for  $\tau/N_{\text{H}}$  agrees well with the DL07 value at  $100\mu\text{m}$ , but at 250 and  $500\mu\text{m}$  the DL07 opacities are smaller, by a factor 1.3 at  $250\mu\text{m}$ , and a factor 1.5 at  $\lambda = 500\mu\text{m}$ . However, we will see below (Section 9) that the shape of the M31 SED seems more consistent with the  $\beta \approx 2.1$  of the DL07 model than the  $\beta \approx 1.8$  favored by (Planck Collaboration et al. 2011).

If the *Planck* opacities are correct, then modeling the FIR emission using the DL07 model will tend to overestimate the dust mass. The present study does not use data longward of  $500\mu\text{m}$ ,

---

<sup>7</sup>Maps of the best-fit values of  $\Sigma_{M_d,j}$ ,  $q_{\text{PAH},j}$ ,  $U_{\min,j}$ ,  $\alpha_j$ , and  $\gamma_j$  at M160 and S350 resolution are available from <http://www.astro.princeton.edu/~draine/m31dust>

so we would not expect this error to be larger than a factor  $\sim 1.3$  (the ratio of the opacities at  $250\mu\text{m}$ ), but the possibility of a systematic error in the dust mass estimate should be kept in mind. Future studies employing the full *Planck* intensity data can be expected to shed further light on dust opacities (Planck Collaboration et al. 2013a,b,c).

Table 3: Far-infrared Absorption/H

$\lambda(\mu\text{m})$	$\tau(\lambda)/N_{\text{H}}$ ( $10^{-25} \text{ cm}^2/\text{H}$ )	
	DL07 Model	Planck Observations <sup>a</sup>
100	5.0	$5.2 \pm 1.6^b$
250	0.75	$1.0 \pm 0.3$
500	0.18	$0.28 \pm 0.08^b$

<sup>a</sup> Planck Collaboration et al. (2011).  
<sup>b</sup> Obtained from  $\tau(250\mu\text{m})/N_{\text{H}}$  assuming  $\beta = 1.8$

### 3.5. Single Pixels versus Annuli

Determination of the dust *mass* requires that the shape of the dust SED be well-determined, so that the dust temperatures can be constrained. With the signal-to-noise properties of the present observations, we do not attempt to estimate the dust mass in a single  $10'' \times 10''$  pixel unless the dust luminosity per unit area (on the sky plane)  $\Sigma_{Ld} > \Sigma_{Ld,\text{min}} = 1.5 \times 10^6 L_{\odot} \text{ kpc}^{-2}$  (IR intensity  $I > 4.8 \times 10^{-5} \text{ erg s}^{-1} \text{ cm}^{-2} \text{ sr}^{-1}$ ). The irregular contour in Figure 1 and the other images bounds the contiguous region with  $\Sigma_{Ld} > \Sigma_{Ld,\text{min}}$  (there are additional pixels with  $\Sigma_{Ld} > \Sigma_{Ld,\text{min}}$  outside this contour).<sup>8</sup> For  $\Sigma_{Ld} \lesssim \Sigma_{Ld,\text{min}}$  the single-pixel dust mass estimates are quite uncertain, especially at S350 resolution where the pixels are smaller, and SPIRE500 and MIPS160 cannot be used. At M160 resolution the larger ( $18'' \times 18''$ ) pixels and inclusion of SPIRE500 and MIPS160 help, but even at M160 resolution the single-pixel dust mass estimates near  $\Sigma_{Ld,\text{min}} = 1.5 \times 10^6 L_{\odot} \text{ kpc}^{-2}$  have substantial uncertainties.

To study radial dependences, we will sometimes take the dust properties obtained by single-pixel modeling and average them over annuli with widths  $10''$  along the minor axis, and  $\Delta R = 46.9''$  (169 pc) along the major axis. While these annuli are not resolved along the minor axis (the MIPS160 FWHM=39''), they are resolved along the major axis.<sup>9</sup>

<sup>8</sup>The boundary contour is established by modeling at M160 resolution (18'' pixels), using all 13 bands to estimate  $\Sigma_{Ld}$ . When modeling at higher resolution (e.g., S350, with 10'' pixels) we continue to use the contours established at M160 resolution to define the ‘‘galaxy mask’’.

<sup>9</sup>If the center of a pixel falls within an annulus, we include the entire pixel in the sums for that annulus – we do not divide pixels that overlap annular boundaries.

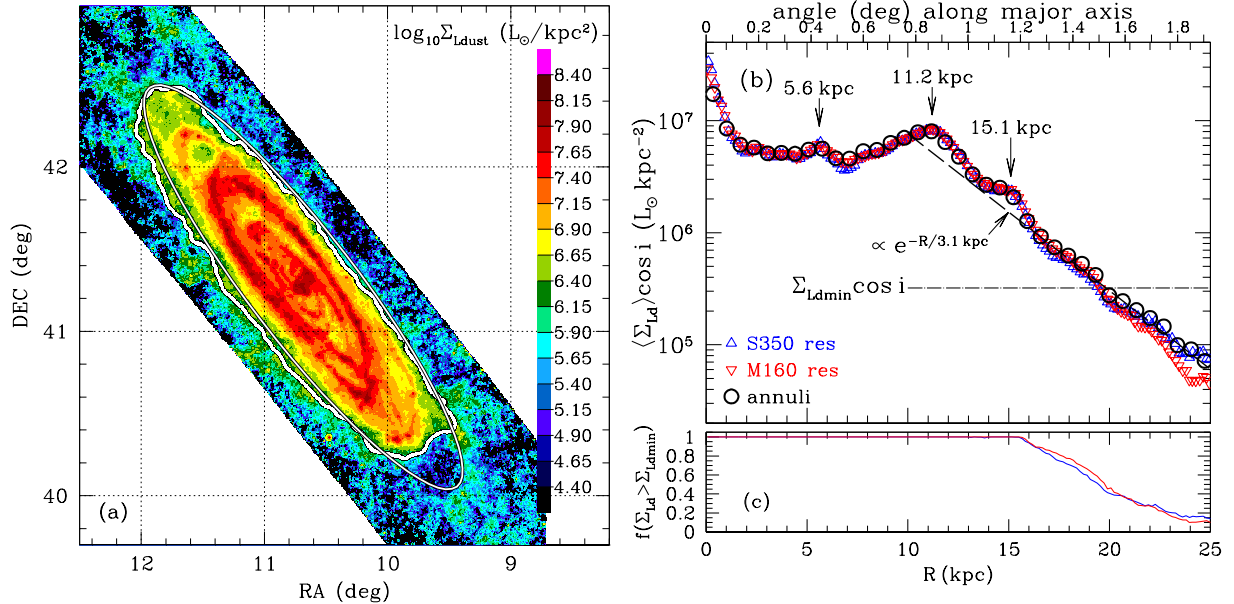


Fig. 2.— (a) Dust luminosity per area on the sky plane  $\Sigma_{Ld}$  at M160 resolution. (b)  $\Sigma_{Ld}$  as a function of radius  $R$ . Triangles: annular average of single-pixel modeling at S350 and M160 resolution. Circles:  $\Sigma_{Ld}$  based on modeling of SED of  $\Delta R = 677$  pc annuli, using all photometric bands. Horizontal dot-dash line: surface brightness below which we do not attempt to model individual pixels. Dashed line: exponential fit (5) for  $R \gtrsim 10$  kpc, with 3.1 kpc scale length. (c) Fraction of pixels at each  $R$  that have  $\Sigma_{Ld} > \Sigma_{Ld, \min}$ . The drop below 100% for  $R > 15.6$  kpc is due to the low  $\Sigma_{Ld}$  area in the SW.

In order to study the dust at  $R > 17$  kpc, where a large fraction of the pixels have  $\Sigma_{Ld} < \Sigma_{Ld, \min}$  (see Figure 2(c)), we use the background-subtracted images to extract the flux in each band from larger concentric annuli with widths  $40''$  along the minor axis, and  $\Delta R = 188''$  ( $677$  pc) along the major axis. These  $\Delta R = 677$  pc annuli are fully resolved, even by MIPS160. The dust mass and starlight intensity distribution in each annulus are then estimated by fitting the SED of the annulus. By integrating over the many pixels in each annulus, the random noise is substantially suppressed. We will see that reliable estimates of the mean dust mass surface density are possible out to  $R \approx 25$  kpc.

#### 4. Dust Luminosity

As described in Aniano et al. (2012), the background-subtracted multiwavelength images are first used to estimate  $\Sigma_{Ld}$ , the total dust luminosity per projected area on the plane of the sky. The luminosity is obtained by fitting a DL07 dust model to the observed fluxes from the pixel, and then integrating over the model SED. While the model dust mass in individual pixels is unreliable for  $\Sigma_{Ld} \lesssim \Sigma_{Ld, \min}$ , the pixel luminosity estimate is reliable down to considerably lower surface brightness. Figure 2(a) shows the dust luminosity surface density  $\Sigma_{Ld}$  at M160 resolution. From

Table 4: Global Quantities for M31<sup>a</sup>

Quantity	$R < 17$ kpc	$17 - 20$ kpc	$20 - 25$ kpc	Total
$L_d (L_\odot)$	$3.98 \times 10^9$	$1.76 \times 10^8$	$1.04 \times 10^8$	$4.26 \times 10^9$
$M_d (M_\odot)$	$4.50 \times 10^7$	$5.25 \times 10^6$	$3.83 \times 10^6$	$5.41 \times 10^7$
$M_H (M_\odot)$	$4.87 \times 10^9$	$8.61 \times 10^8$	$9.83 \times 10^8$	$6.71 \times 10^9$
$\langle q_{\text{PAH}} \rangle_{\text{MMP83}}$	0.0364			
$\langle q_{\text{PAH}} \rangle_{\text{corr}}$	0.0391			
$M_d/M_H$	0.00924	0.00610	0.00390	0.00806

<sup>a</sup>  $D = 744$  kpc, inclination  $i = 77.7^\circ$

the image it can be seen by eye that the dust luminosity is detectable down to  $\Sigma_{L_d} \approx 10^{5.9} L_\odot \text{ kpc}^{-2}$ .

The mean luminosity per area as a function of radius is found by averaging the single-pixel luminosities over the  $\Delta R = 177$  pc annuli. Figure 2(b) shows  $\Sigma_{L_d} \cos i$ , the dust luminosity surface density on the disk plane, averaged over the  $\Delta R = 177$  pc annuli, and plotted against the annular radius  $R$ . Triangles show annular averages of single-pixel results obtained at M160 resolution (using all cameras) and at S350 resolution (not using SPIRE500 or MIPS160). Circles show results of modeling the SED of  $\Delta R = 677$  pc annuli. The smooth decline in  $\Sigma_{L_d}$  with increasing  $R$  out to  $R \approx 23$  kpc is an indication that background subtraction has been reasonably successful at least down to surface brightnesses  $\Sigma_{L_d} \approx 4 \times 10^5 L_\odot \text{ kpc}^{-2}$  ( $\Sigma_{L_d} \cos i \approx 8 \times 10^4 L_\odot \text{ kpc}^{-2}$ ).

Figure 2(c) shows the fraction  $f$  of the pixels at each  $R$  that have  $\Sigma_{L_d} > \Sigma_{L_d, \text{min}}$ . The fraction  $f = 1$  for  $R < 15$  kpc, but at  $R \approx 15.6$  kpc the fraction begins to fall. At  $R \approx 24$  kpc the fraction has fallen to  $f \approx 0.1$ ; some fraction of these pixels may be raised above  $\Sigma_{L_d, \text{min}}$  by unresolved background galaxies.

The dust luminosity surface density  $\Sigma_{L_d}$  derived from the SEDs of  $\Delta R = 677$  pc annuli, shown in Figure 2(b), is in good agreement with  $\Sigma_{L_d}$  obtained from pixel-based modeling. From the annular SEDs, the dust luminosity surface density for  $17 \text{ kpc} < R < 25 \text{ kpc}$  is

$$\Sigma_{L_d} \cos i \approx 8.0 \times 10^5 \exp[-(R - 17 \text{ kpc})/3.1 \text{ kpc}] L_\odot \text{ kpc}^{-2} \quad . \quad (5)$$

For purposes of estimating the integrated dust properties from the pixel-based modeling, we sum over the M160 pixel-based modeling for  $R < 17$  kpc, and use the annular SED modeling for  $R > 17$  kpc (see Table 4). We estimate the  $R < 25$  kpc dust luminosity to be  $L_d = 4.26 \times 10^9 L_\odot$ .

Because  $\nu L_\nu$  peaks near  $100 \mu\text{m}$ , the global dust luminosity of M31 was already reasonably well-determined by the low-resolution observations by *IRAS* (60,  $100 \mu\text{m}$ ) and *COBE* (140,  $240 \mu\text{m}$ ). Adding  $175 \mu\text{m}$  imaging by *ISO*, Haas et al. (1998) obtained  $L_d \approx 3.8 \times 10^9 L_\odot$ .<sup>10</sup> Using MIPS

<sup>10</sup>All luminosities have been corrected to  $D = 744$  kpc

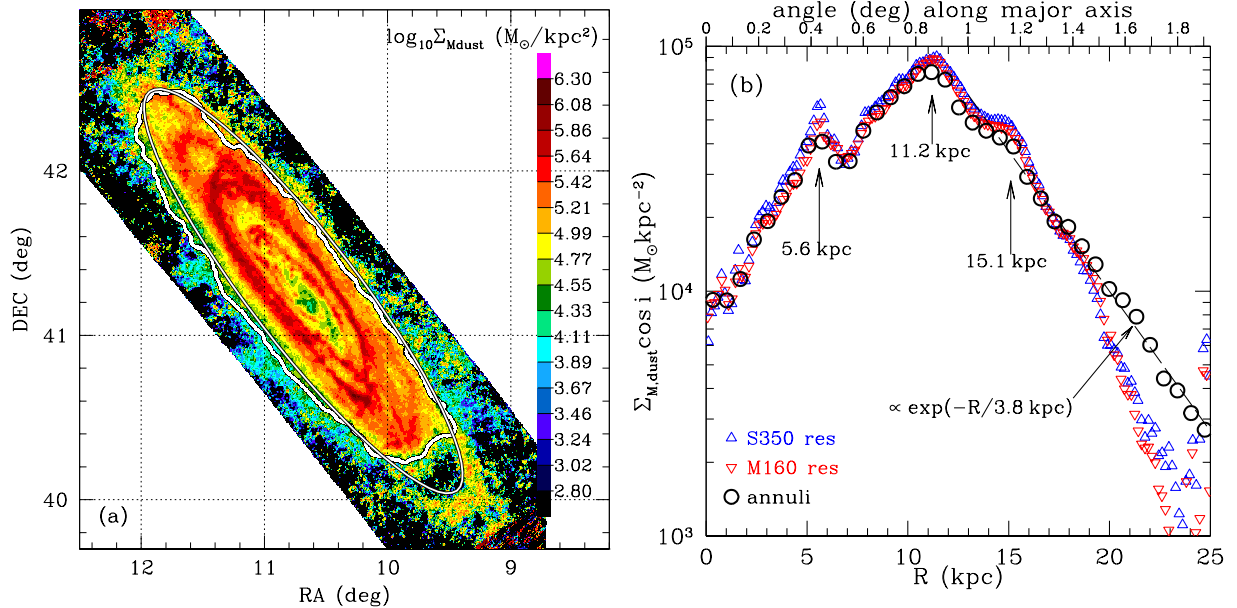


Fig. 3.— (a) Map of dust mass surface density  $\Sigma_{M_d}$  at M160 resolution. The irregular contour delineates the contiguous region with  $\Sigma_{L_d} > \Sigma_{L_d, \min}$ ; outside of this contour, the dust map is unreliable. (b) Radial profile of  $\Sigma_{M_d}$  projected onto the M31 disk plane, for  $\cos i = 0.213$ . Triangles: annular average of  $\Sigma_{M_d}$  from single-pixel modeling at S350 and M160 resolution. For each  $R$ ,  $\Sigma_{M_d}$  is the average for pixels with  $\Sigma_{L_d} > \Sigma_{L_d, \min}$ . Circles:  $\Sigma_{M_d}$  obtained by modeling SED of  $\Delta R = 677$  pc annuli, using all bands.

photometry, Gordon et al. (2006) found  $L_d \approx 4.0 \times 10^9 L_\odot$ , consistent, within the uncertainties, with the present value of  $L_d = 4.26 \times 10^9 L_\odot$ .

There is considerable structure in the dust luminosity image in Figure 2(a), with close similarities to the SPIRE  $350\mu\text{m}$  image in Figure 1. While the structure is not purely “circular” (on the plane of the galaxy), the dust luminosity density extracted in (inclined) circular annuli centered on the dynamical center, shown in Figure 2(b), exhibits a strong central peak (due to small amounts of relatively warm dust), two clear rings (at  $R = 5.6$  kpc and  $R = 11.2$  kpc) and indications of a third ring (at  $R \approx 15.1$  kpc). The 11.2 kpc ring was evident in the original *IRAS* imaging (Habing et al. 1984), and all three rings were noted in the *ISO*  $175\mu\text{m}$  imaging by Haas et al. (1998).

## 5. Dust Mass, Dust-to-Gas Ratio, and Metallicity

### 5.1. Dust Mass

Before the launch of *Herschel Space Observatory*, the mass of dust in M31 had been estimated by Xu & Helou (1996), Haas et al. (1998), and Gordon et al. (2006) (see Table 5). With *Herschel* imaging out to  $500\mu\text{m}$ , we are now able to obtain improved estimates for the total dust mass, and

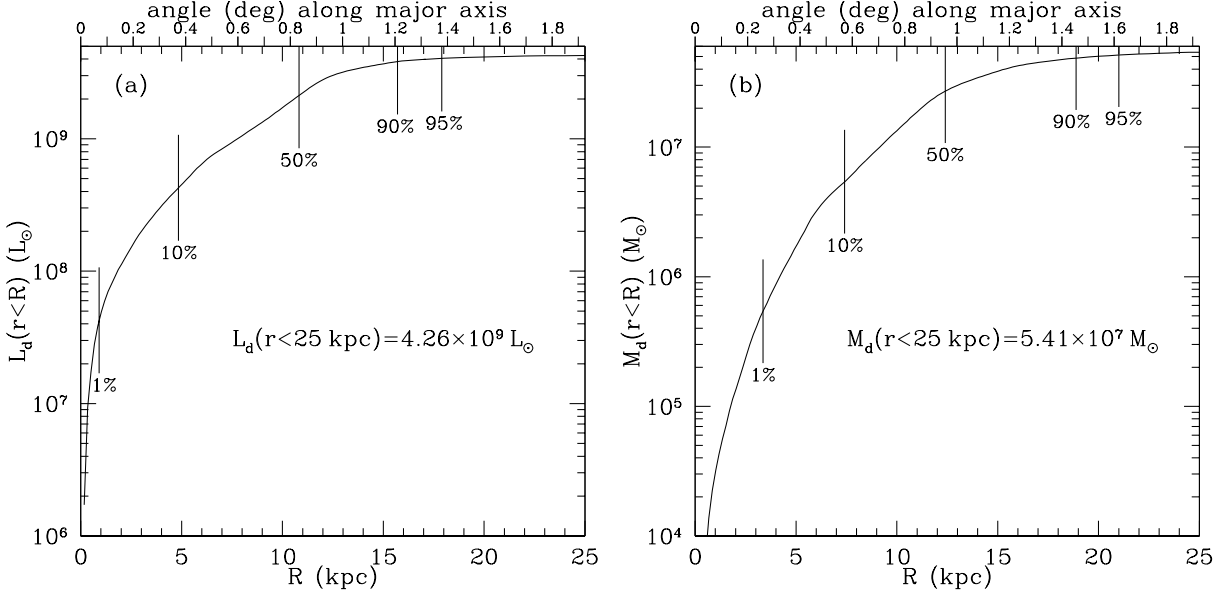


Fig. 4.— (a) Dust luminosity interior to radius  $R$ , showing radii containing 1%, 10%, 50%, 90%, and 95% of the total dust luminosity within 25 kpc. (b) Dust mass interior to radius  $R$ , showing radii containing 1%, 10%, 50%, 90%, and 95% of the total dust mass interior to 25 kpc. For  $R < 17$  kpc  $L_d(r < R)$  and  $M_d(r < R)$  are based on single-pixel modeling at M160 resolution; for  $17 \text{ kpc} < R < 25$  kpc the results are based on modeling the SEDs of  $\Delta R = 677$  pc annuli.

to map the dust out to  $\sim 20$  kpc. Figure 3(a) shows the dust mass surface density  $\Sigma_{M_d}$  on the plane of the sky, obtained by modeling at M160 resolution.

In addition to constructing maps showing the dust properties in every pixel, we also average the dust properties over rings that are circular on the disk plane in order to study radial trends. For each annulus, we calculate the mean dust mass surface density obtained by summing the dust masses in pixels with  $\Sigma_{L_d} > \Sigma_{L_d, \text{min}}$ , dividing by the total area of the annulus. For  $R < 15.6$  kpc all pixels have  $\Sigma_{L_d} > \Sigma_{L_d, \text{min}}$ , but this procedure will underestimate the actual mean surface density for  $R > 16$  kpc. Figure 3(b) shows the dust mass surface density projected onto the M31 disk plane, as a function of galactocentric radius  $R$ . Triangles show annular averages of single-pixel modeling at S350 resolution (MIPS160 and SPIRE500 not used) and at M160 resolution (using all the data). Dust mass surface densities obtained at S350 resolution (not using MIPS160 and SPIRE500) agree to within  $\sim 10\%$  with dust mass estimates obtained at M160 resolution, using all cameras.

Dust mass surface densities  $\Sigma_{M_d}$  estimated by fitting SEDs of  $\Delta R = 677$  pc annuli are shown (open circles) in Figure 3(b), and are seen to agree to within  $\sim 10\%$  with the results of the pixel-based modeling for  $R < 15$  kpc where the signal-to-noise is high. For  $R > 16$  kpc, where a growing fraction of pixels has  $\Sigma_{L_d} < \Sigma_{L_d, \text{min}}$ , the annular SED is the best way to estimate the dust mass. The dust mass surface density at  $R > 17$  kpc is seen to be approximated by the broken line in

Figure 3b:

$$\Sigma_{M_d} \cos i \approx 2.2 \times 10^4 \exp[-(R - 17 \text{ kpc})/3.8 \text{ kpc}] M_\odot \text{ kpc}^{-2} \quad \text{for } R > 17 \text{ kpc}. \quad (6)$$

The dust mass surface density in Figure 3(b) shows two distinct peaks, corresponding to rings at  $R = 5.6 \text{ kpc}$  and  $R = 11.2 \text{ kpc}$ , with a third ring at  $R = 15.1 \text{ kpc}$ . The  $11.2 \text{ kpc}$  ring coincides with a peak in the H I 21cm emission, a ring of star formation (seen in H $\alpha$ ; Devereux et al. 1994), and a  $\sim 40\%$  overdensity of stars with ages  $> 1 \text{ Gyr}$  (Dalcanton et al. 2012). The image of the dust mass surface density in Figure 3(a) shows a conspicuous deficiency of dust between  $\sim 16\text{--}20 \text{ kpc}$  on the SW side of the disk. As will be discussed further below, this is not an artifact – the H I gas shows a similar deficiency in the same region.

The DL07 dust model has<sup>11</sup>

$$A_V = 0.74 \left( \frac{\Sigma_{M_d}}{10^5 M_\odot \text{ kpc}^{-2}} \right) \text{ mag} \quad . \quad (7)$$

At  $R \approx 20 \text{ kpc}$ , the dust mass surface density (projected onto the disk of M31)  $\Sigma_{M_d} \cos i \approx 9 \times 10^3 M_\odot \text{ kpc}^{-2}$ , corresponds to a visual extinction  $A_V \approx 0.07 \text{ mag}$  normal to the disk of M31, or  $A_V \approx 0.3 \text{ mag}$  along our line-of-sight. The peak dust mass surface density occurs at  $R = 11.2 \text{ kpc}$  with a dust surface density, projected onto the M31 disk,  $\Sigma_{M_d} \cos i \approx 7 \times 10^4 M_\odot \text{ kpc}^{-2}$ , corresponding to  $A_V \approx 0.5 \text{ mag}$  normal to the disk ( $A_V \approx 2.4 \text{ mag}$  along our line-of-sight). Many pixels in Figure 3 have higher dust surface densities, reaching  $\Sigma_{M_d} \approx 10^{6.0} M_\odot \text{ kpc}^{-2}$ , corresponding to  $A_V \approx 7 \text{ mag}$ . In these pixels the dust is presumably distributed inhomogeneously. *Hubble Space Telescope* observations of M31 (Dalcanton et al. 2012) may allow measurement of reddening toward many individual stars in M31; it will be of great interest to compare the stellar reddening values with the present maps of dust surface density.

We consider our best estimate for the dust mass to be the dust mass obtained using all cameras (including MIPS160). For  $R < 17 \text{ kpc}$  we use the M160 resolution single-pixel estimates for  $\Sigma_{M_d}$ , while for  $R > 17 \text{ kpc}$  we use the annular SEDs to estimate the dust mass in each annulus. We find a total dust mass  $M_d = 5.4 \times 10^7 M_\odot$  within  $R = 25 \text{ kpc}$  (see Table 4).

It is difficult to estimate objectively the uncertainty in the estimate for  $M_d$ . Calibration uncertainties in the photometry itself are at least 10% for each of the MIPS, PACS, and SPIRE bands. The inconsistencies between MIPS and PACS at  $70 \mu\text{m}$  and  $160 \mu\text{m}$  are larger than expected (see Appendix A), and, in addition, there are difficult-to-assess errors arising from assumptions made in the modeling about the physical properties of the dust, and simplified treatments of the starlight intensity distribution. Overall, we adopt a tentative uncertainty estimate of 20% for the global dust mass given in Tables 4 and 5.

---

<sup>11</sup> The coefficient 0.74 differs from the value 0.67 in Aniano et al. (2012) because of the mass renormalization discussed in Section 3.2.

Figure 4 shows the cumulative dust luminosity and dust mass as a function of  $R$ . We find that half of the dust mass in M31 lies at  $R > 12.3$  kpc, and  $> 10\%$  lies beyond 19 kpc.

Table 5: Estimates for the Dust Mass in M31

$M_d(10^7 M_\odot)^a$	Data used	Reference
$2.2 \pm 0.7$	<i>IRAS</i> , extinction, H I	Xu & Helou (1996)
$3.5 \pm 1.0$	<i>IRAS</i> 100, COBE-DIRBE 140,240, ISO 175 $\mu$ m	Haas et al. (1998)
4	<i>IRAS</i> , COBE-DIRBE, <i>ISO</i> , MIPS	Gordon et al. (2006)
$5.05 \pm 0.45$	PACS 100,160; SPIRE 250,350,500; annuli	HELGA I Fritz et al. (2012)
2.6	PACS 100,160; SPIRE 250,350,500; S500 pixels	HELGA II Smith et al. (2012)
<b><math>5.4 \pm 1.1</math></b>	<b>MIPS, PACS, SPIRE</b> ; M160 pixels and annuli	<b>This work</b>

<sup>a</sup> For  $D = 744$  kpc.

The HELGA survey (Fritz et al. 2012; Smith et al. 2012) obtained PACS and SPIRE imaging of M31 at a scan speed of  $60'' s^{-1}$  (three times faster than the scan speed for the PACS and SPIRE imaging used in the present study). HELGAI (Fritz et al. 2012) measured the fluxes in a central circular aperture and five concentric annuli extending out to 20 kpc. Except for the central circle, the annular boundaries were ellipses. The  $\lambda \geq 100\mu$ m SED of each annulus was fit with a modified blackbody  $F_\nu \propto \nu^\beta B_\nu(T)$ , with fixed  $\beta = 1.8$ . The total dust mass  $M_d = (5.05 \pm 0.45) \times 10^7 M_\odot$  found within 20 kpc by HELGAI is close to the present estimate  $M_d(R < 20 \text{ kpc}) = (5.0 \pm 1.0) \times 10^7 M_\odot$ .

HELGA II (Smith et al. 2012) restricted their study to pixels satisfying their criterion of  $5\sigma$  detection in each of six bands (MIPS70, PACS100, PACS160, and the SPIRE bands). The MIPS70 photometry was used only as an upper limit: a modified blackbody  $A\nu^\beta B_\nu(T)$  was used, with  $A$ ,  $\beta$ , and  $T$  adjusted to fit the 100–500 $\mu$ m photometry for each pixel; models for the cool dust were acceptable provided they did not exceed the MIPS70 photometry. In the regions included in their study, HELGA II found a total dust mass  $M_d = 2.6 \times 10^7 M_\odot$ , but Smith et al. (2012) note that the pixels satisfying their  $5\sigma$  criterion accounted for only  $\sim 50\%$  of the global 500 $\mu$ m emission from M31.

## 5.2. Dust-to-gas Ratio and Metallicity

Braun et al. (2009) mapped the H I 21 cm emission out to  $\sim 25$  kpc from the center of M31. After correcting for self-absorption, they obtained a map of the H I surface density, which we use here. Integrating this map out to  $R = 25$  kpc yields an H I mass  $M(\text{HI}) = 6.38 \times 10^9 M_\odot$  (88% of the total H I in their map). CO (1–0) has been mapped out to  $\sim 12$  kpc, with the associated H<sub>2</sub>



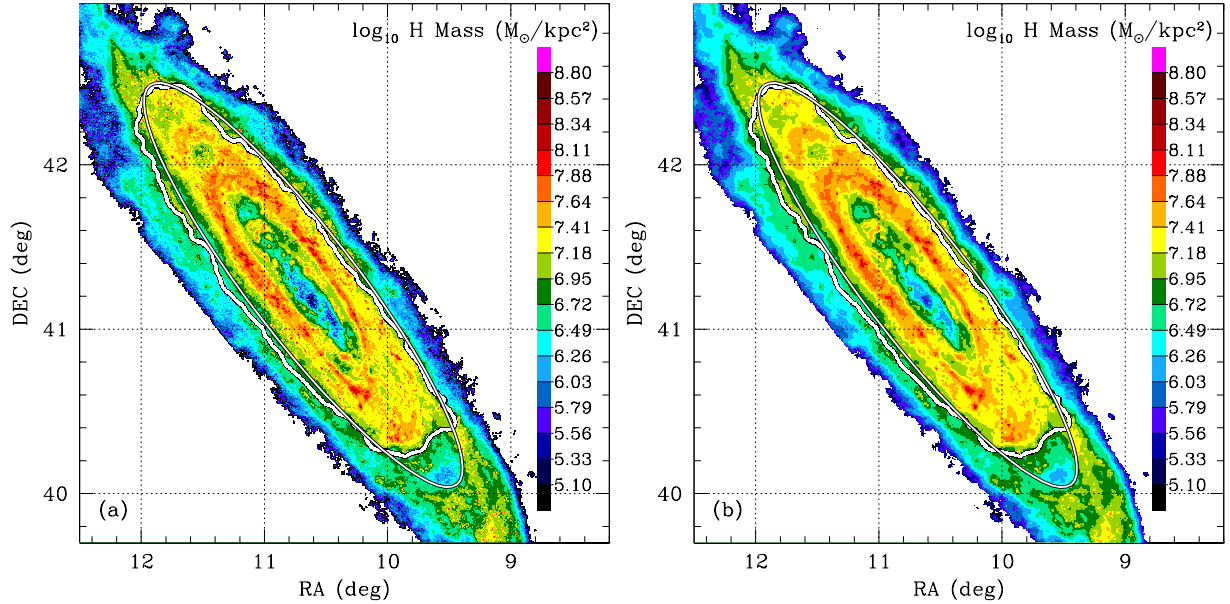


Fig. 5.— Surface density  $\Sigma_{\text{H}} = \Sigma(\text{HI}) + \Sigma(\text{H}_2)$  from HI 21cm (Braun et al. 2009) and CO 1-0 (Nielen et al. 2006, using  $X_{\text{CO}} = 2 \times 10^{20} \text{ cm}^{-2} (\text{K km s}^{-1})^{-1}$ ) at S350 resolution (left) and M160 resolution (right). Most of the structure seen at S350 resolution survives at M160 resolution. Note the deficiency of gas in the SW at radii  $15 \text{ kpc} < R < 20 \text{ kpc}$ .

mass estimated<sup>12</sup> to be  $M(\text{H}_2) \approx 3.4 \times 10^8 M_{\odot}$  (Nielen et al. 2006). We take the total H surface density to be  $\Sigma_{\text{H}} \approx \Sigma(\text{HI}) + \Sigma(\text{H}_2)$ , where  $\Sigma(\text{H}_2)$  is obtained from the observed CO 1-0 emission assuming a constant  $X_{\text{CO}} = 2 \times 10^{20} \text{ H}_2 \text{ cm}^{-2} (\text{K km s}^{-1})^{-1}$ .

We may be underestimating  $\Sigma_{\text{H}}$ .  $\text{H}_2$  that is “CO dark” (i.e., not associated with CO 1-0 emission) is assumed to be a small fraction of the total  $\text{H}_2$  mass. More importantly, we do not include H II gas in our estimate for  $\Sigma_{\text{H}}$ . The ionized gas mass in bright H II regions is small, but the mass in low-density diffuse H II may not be negligible. For our Galaxy, it is estimated that diffuse H II accounts for  $\sim 23\%$  of the total ISM mass at  $R < 20 \text{ kpc}$  (Draine 2011b). The center of M31 has  $\Sigma_{\text{H}} \approx 1.8 \times 10^6 M_{\odot} \text{ kpc}^{-2}$  averaged over  $R < 1 \text{ kpc}$ . The extinction-corrected surface brightness of  $\text{H}\alpha \sim 2 \times 10^{-5} \text{ erg cm}^{-2} \text{ s}^{-1} \text{ sr}^{-1}$  (Devereux et al. 1994; Tabatabaei & Berkhuijsen 2010) corresponds to an H II surface density  $6 \times 10^6 (\text{cm}^{-3} / \langle n_e \rangle) T_4^{0.94} M_{\odot} \text{ kpc}^{-2}$ , where  $\langle n_e \rangle$  is the electron density within the emitting regions. The density-sensitive [S II]6716/[S II]6731 line ratio indicates  $\langle n_e \rangle > 1.2 \times 10^2 \text{ cm}^{-3}$  for  $R \lesssim 0.2 \text{ kpc}$  (Ciardullo et al. 1988), hence the mass in  $\sim 10^4 \text{ K}$  plasma appears to be small compared to that in neutral gas. X-ray observations indicate that  $R \lesssim 1 \text{ kpc}$  is filled with hot gas with  $T \approx 4 \times 10^6 \text{ K}$  and a mean surface density  $\sim 2 \times 10^5 M_{\odot} \text{ kpc}^{-2}$  (Bogdán & Gilfanov 2008), only  $\sim 10\%$  of the  $R < 1 \text{ kpc}$  H I mass.

<sup>12</sup> Using a conversion factor  $X_{\text{CO}}(J = 1 \rightarrow 0) = 2 \times 10^{20} \text{ H}_2 \text{ cm}^{-2} (\text{K km s}^{-1})^{-1}$  (Bolatto et al. 2013).

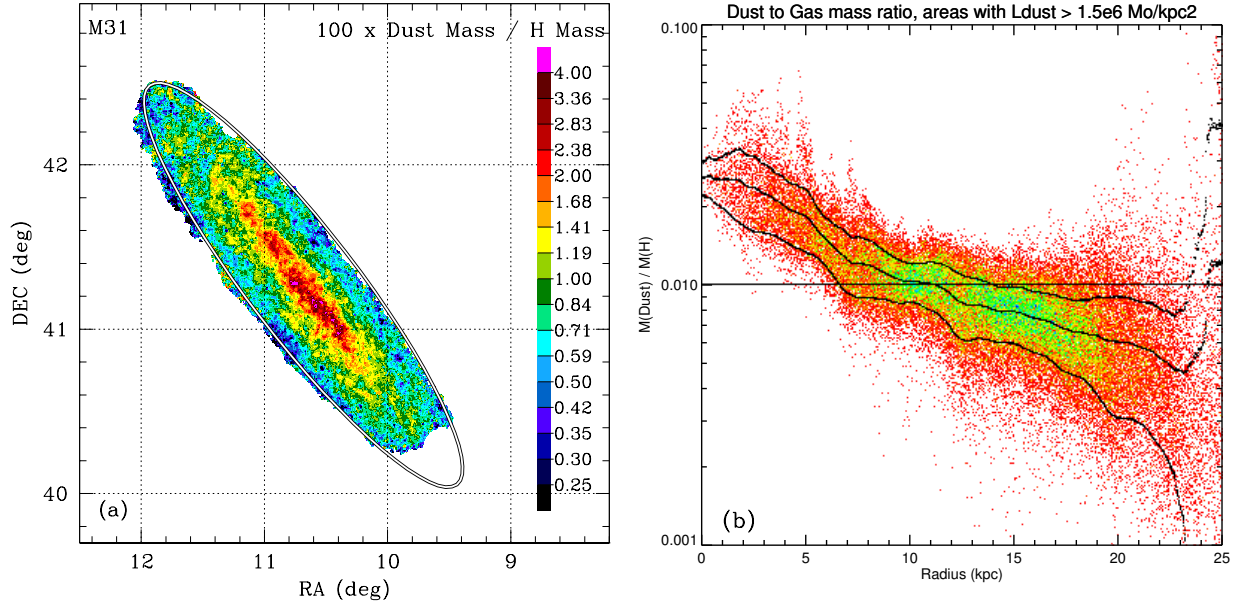


Fig. 6.— (a) Dust-to-H mass ratio at M160 resolution, for pixels within the  $\Sigma_{Ld} = \Sigma_{Ld,\min}$  contour. (b) Dust-to-H mass ratio for each M160 resolution pixel with  $\Sigma_{Ld} > \Sigma_{Ld,\min}$ . The central curve is the mean in each radial bin; the other curves are the mean  $\pm \sigma$ , where  $\sigma^2$  is the estimated variance of the distribution.

It is also possible that we may have overestimated  $\Sigma_H$  in the center – Leroy et al. (2011) find that  $X_{CO}$  in the center ( $R < 2$  kpc) of M31 is lower by about a factor two. However, there is little CO emission at  $R \lesssim 2$  kpc (Nielen et al. 2006), hence the total gas mass there is insensitive to uncertainties in  $X_{CO}$ .

Figure 5 shows  $\Sigma_H$  at S350 and M160 resolution. Note the deficiency of gas in the SW for  $R > 15.6$  kpc; the same region is also seen (see Figure 2) to be deficient in emission from dust. The reason for the deficiency in dust and gas in the SW corner of M31 (between  $R = 16$  and  $R \approx 20$  kpc) is not known, but this part of the M31 disk has the appearance of having been affected by some recent event. Block et al. (2006) argued that a nearly head-on collision with M32  $\sim 210$  Myr ago can account for the observed offset of the center of the 11 kpc ring, but such an encounter would not seem likely to produce the observed deficiency of H I and dust in the SW at  $R \approx 16 - 20$  kpc. It may be the result of an encounter with another member of the Local Group within the past Gyr. Lewis et al. (2013) discuss the Giant Stellar Stream, extending from the SW side of the disk toward M33. H I 21 cm observations also show a diffuse gaseous filament connecting M31 and M33, including a feature extending from the SW side of the M31 disk toward M33. The origin of the Giant Stellar Stream and the H I filamentary structure is uncertain, but strongly suggestive of a close passage of M33, possibly accounting for the deficiency of interstellar matter on the SW side of the disk,  $\sim 18$  kpc from the center of M31.

Figure 6(a) is a map of the dust-to-H mass ratio at M160 resolution. Some azimuthal structure

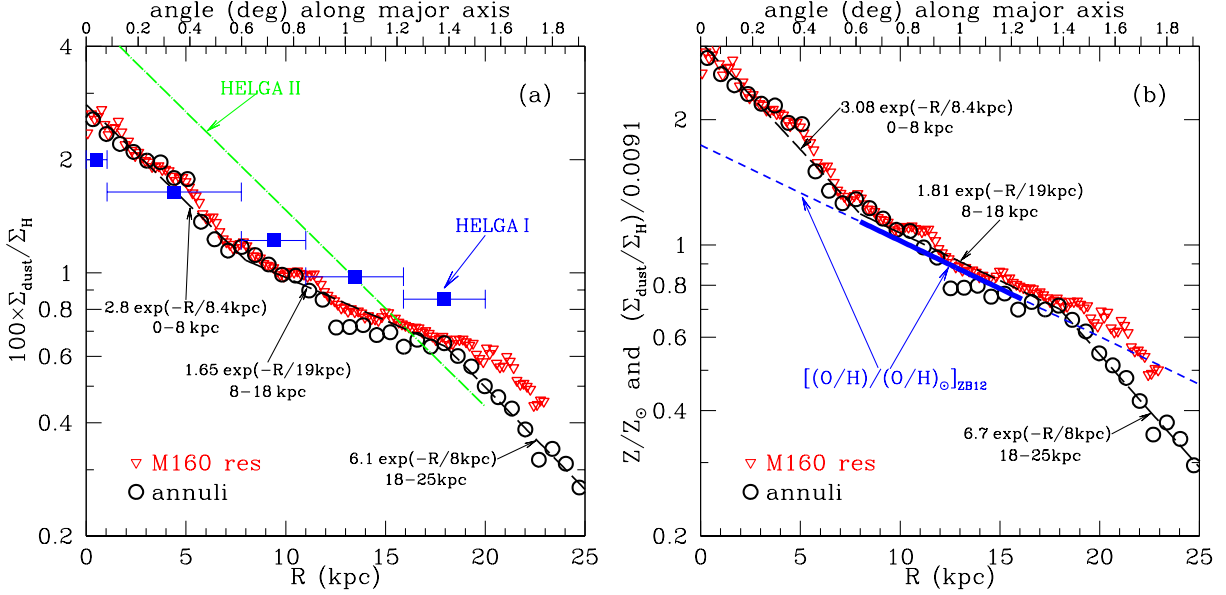


Fig. 7.— (a)  $100 \times \text{dust}/\text{H}$  mass ratio in M31 as a function of galactocentric radius  $R$ . Triangles: present work, modeling at M160 resolution, using only pixels with  $\Sigma_{Ld} > \Sigma_{Ld,\text{min}}$ . Circles: present work, modeling the SED for  $\Delta R = 677 \text{ pc}$  annuli. Squares: HELGAI (Fritz et al. 2012). Dot-dash line: HELGAII (Smith et al. 2012). (b) Metallicity relative to solar, based on our dust modeling (triangles and circles, as in (a)), and H II region oxygen abundances (Zurita & Bresolin 2012); the line is shown as solid in the 8–16 kpc range where the oxygen abundances are from the “direct” method.

is evident, but the main feature is a conspicuous radial trend, with the dust-to-H ratio peaking at the center and declining with  $R$ . Figure 6(b) shows results for every pixel (at M160 resolution) satisfying the condition  $\Sigma_{Ld} > \Sigma_{Ld,\text{min}}$ . Because of the low signal/noise ratio (S/N) in individual pixels, the scatter in the derived  $M_d/M_H$  is quite pronounced for  $R \gtrsim 17 \text{ kpc}$ . However, the mean dust/H ratio in each annulus exhibits a clear trend, decreasing with increasing  $R$ . The central dust-to-H ratio is  $M_d/M_H \approx 0.028$ , declining to  $\sim 0.005$  at  $R \approx 20 \text{ kpc}$ : a factor of  $\sim 5$  change in the dust-to-H ratio moving from the center to  $R \approx 20 \text{ kpc}$ .

Figure 7 (triangles) shows the radial profile of the dust-to-H ratio estimated at M160 resolution. Each triangle in Figure 7 is obtained by summing the M160 resolution dust and gas within rings for  $R < 23 \text{ kpc}$ , including only pixels satisfying the criterion  $\Sigma_{Ld} > \Sigma_{Ld,\text{min}}$ , and calculating the ratio of (total dust)/(total gas) for that ring. The dust/gas ratio therefore applies only to the pixels satisfying the  $\Sigma_{Ld} > \Sigma_{Ld,\text{min}}$  cut. From Figure 2(b) we see that essentially 100% of the pixels at  $R < 16 \text{ kpc}$  satisfy the surface brightness cut. However, at  $R = 20 \text{ kpc}$ ,  $\sim 50\%$  of the pixels in the annulus do not satisfy the cut. This incompleteness is due in part to the general radial decline in surface brightness, but in part it reflects the conspicuous deficit of both gas and dust in the SW corner of M31. Also shown in Figure 7 (circles) is the dust-to-H mass ratio estimated for  $\Delta R = 677 \text{ pc}$  annuli, where the dust mass is obtained by modeling the SED of each annulus, and

the gas mass is the total mass of gas within the annulus. The dust-to-gas ratio is well-behaved out to 25 kpc. For  $R < 18$  kpc the dust-to-H mass ratio estimates for the  $\Delta R = 677$  pc annuli at  $R = 16 - 23$  kpc are in good agreement with the dust-to-H mass ratios determined only for the pixels with  $\Sigma_{Ld} > \Sigma_{Ld,\min}$ . For  $R > 18$  kpc the dust/gas ratios for the pixels with  $\Sigma_{Ld} > \Sigma_{Ld,\min}$  is somewhat higher than the result from the annular photometry. This bias is attributable to the fact that for  $\Sigma_{Ld}$  just below  $\Sigma_{Ld,\min}$ , noise can raise the pixel above the threshold, leading to overestimation of the dust mass. In this regime, dust mass estimates from the annular photometry and modeling should be more reliable.

We find that the dust/H ratio for 0–25 kpc declines monotonically with increasing  $R$ , with

$$\frac{M_d}{M_H} \approx \begin{cases} 0.0280 \exp(-R/8.4 \text{ kpc}) & R < 8 \text{ kpc} \\ 0.0165 \exp(-R/19 \text{ kpc}) & 8 \text{ kpc} < R < 18 \text{ kpc} \\ 0.0605 \exp(-R/8 \text{ kpc}) & 18 \text{ kpc} < R \lesssim 25 \text{ kpc} \end{cases} , \quad (8)$$

shown as a dashed line in Figure 7. Also shown in Figure 7(a) is the dust/gas ratio estimated by HELGA I (Fritz et al. 2012) for each of 5 radial zones. The HELGA I results are in fair agreement with our findings interior to  $\sim 8$  kpc, but at larger radii tend to exceed our dust mass estimates.

HELGA II (Smith et al. 2012) conclude that the dust/H ratio follows an exponential profile in M31, with  $M_{\text{dust}}/M_H \approx 0.049 \exp(-R/8.7 \text{ kpc})$ ; this is plotted in Figure 7(a). Our central dust/H ratio  $\sim 0.028$  is only 60% of the value found by HELGA II.

## 6. Metallicity of the ISM in M31

If depletions are similar to the local Milky Way, we expect

$$\frac{M_d}{M_H} \approx 0.0091 \frac{Z}{Z_\odot} . \quad (9)$$

where  $Z$  is the mass fraction of elements other than H and He. This allows us to estimate the metallicity from our measured dust/H mass ratio (8):

$$\frac{Z}{Z_\odot} \approx \begin{cases} 3.08 \exp(-R/8.4 \text{ kpc}) & R < 8 \text{ kpc} \\ 1.81 \exp(-R/19 \text{ kpc}) & 8 \text{ kpc} < R < 18 \text{ kpc} \\ 6.65 \exp(-R/8 \text{ kpc}) & 18 \text{ kpc} < R \lesssim 25 \text{ kpc} \end{cases} . \quad (10)$$

This relation is plotted in Figure 7(b).

Zurita & Bresolin (2012, hereafter ZB12) measured elemental abundances in M31 H II regions using “direct” methods between 8 and 16 kpc. When they allow for depletion of oxygen into grains and a bias against H II regions with high oxygen abundances, they estimate that

$$(\text{O}/\text{H}) \approx 1.8(\text{O}/\text{H})_\odot \exp(-R/19 \text{ kpc}) . \quad (11)$$

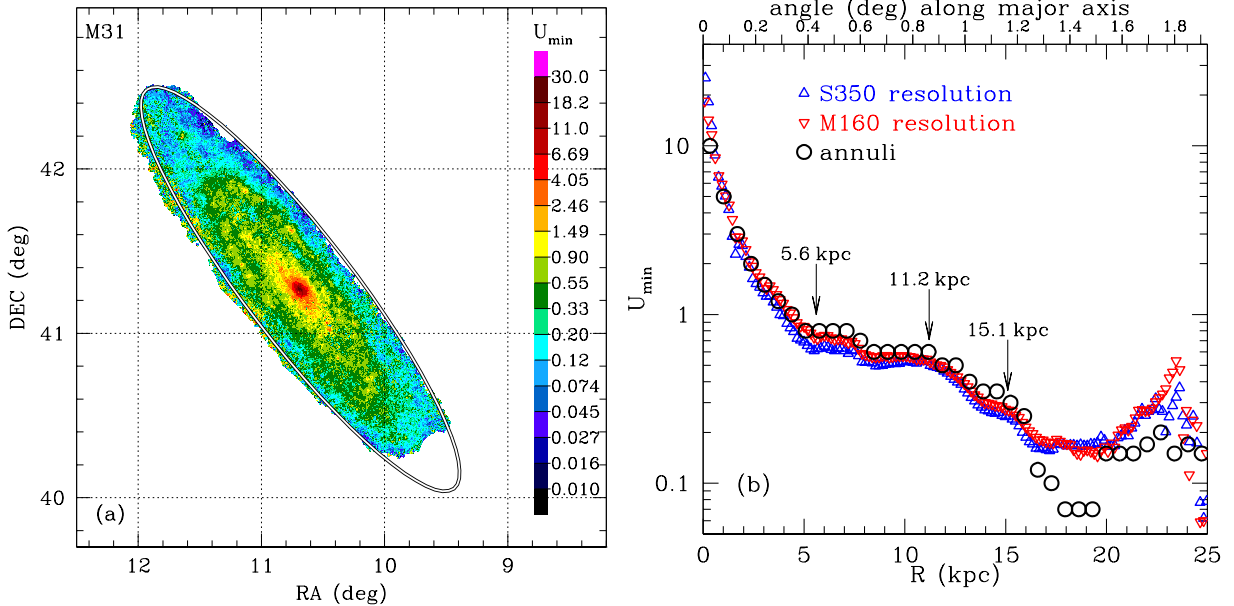


Fig. 8.— (a) Starlight heating rate parameter  $U_{\min}$  in M31 at S350 resolution. (b) Radial profile of  $U_{\min}$ , estimated at S350 resolution and M160 resolution (triangles) and using annular photometry (circles). Locations of dust mass surface density maxima are indicated.

However, it is important to note that the H II region abundance determinations have appreciable uncertainties, and do not agree well with metallicity determinations in the atmospheres of B supergiants. Our result (Equation (10)) for the metallicity is in excellent agreement with the ZB12 metallicity over the  $8 \text{ kpc} < R < 16 \text{ kpc}$  range where the ZB12 H II region metallicities were based on direct determinations of the gas temperature, and are therefore most reliable.

According to Equation (10), the ISM in M31 has supersolar abundances for  $R \lesssim 11 \text{ kpc}$ . This is consistent with the high WC/WN stellar ratio observed in M31 (Neugent et al. 2012).

## 7. Dust Temperature and Starlight Properties

If the distribution of both stars and dust were known, the intensity and spectrum of the starlight heating the dust could be obtained from the equations of radiative transfer (see, e.g., Popescu & Tuffs 2013). In dusty star-forming galaxies this is a formidable problem, because of the complex and correlated spatial distributions of both stars and dust.

To model the infrared emission from dust, we take a much simpler approach, empirical approach to the starlight heating. Within a single “pixel” (which may include  $\sim 10^4 \text{ pc}^2$  of disk area) the dust may be exposed to a wide range of starlight intensities, ranging from the general starlight background in the diffuse ISM, to high intensities found in star-forming regions. The DL07 model

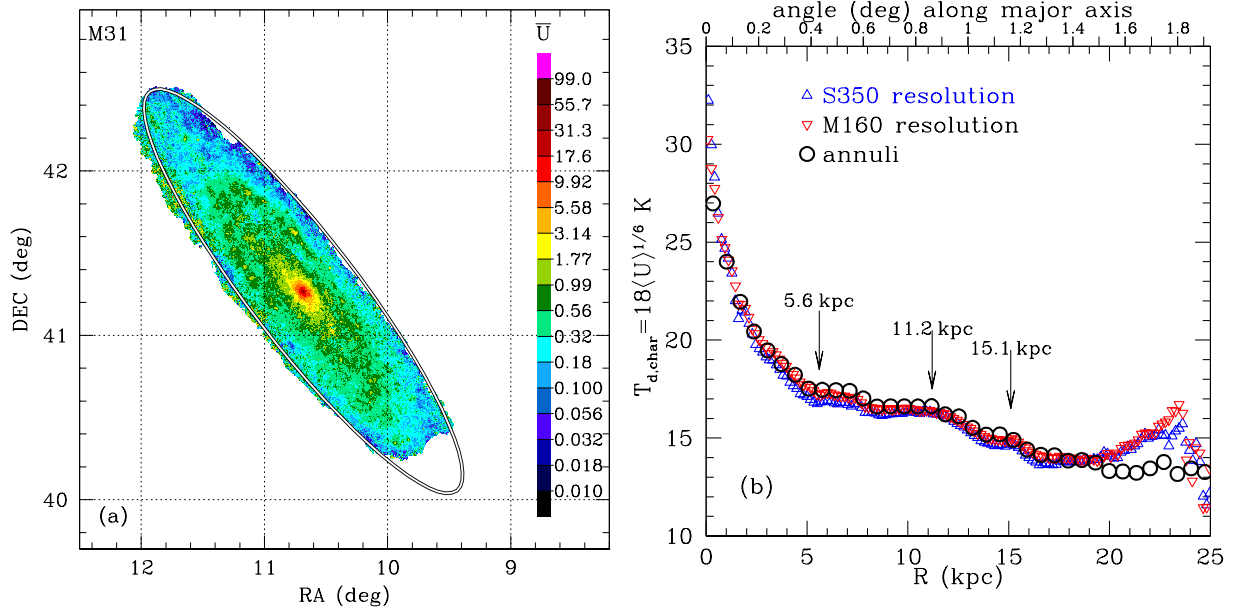


Fig. 9.— Left: map of mean starlight heating rate parameter  $\langle U \rangle = \bar{U}$  in M31 at S350 resolution. Right: radial profile of characteristic dust temperature. Locations of dust surface density maxima are indicated.

adopts a parameterized distribution function for the starlight heating rate: the dust within a given pixel is assumed to be subject to starlight heating rates ranging from  $U = U_{\min}$  to a peak value  $U_{\max} = 10^7$ , with an intensity distribution given by Equation (4). When fitting the dust model to the data, we in effect use the dust grains as photometers to determine the intensity of starlight in the regions where dust is present. The parameter  $U_{\min}$  is interpreted as being the starlight heating rate in the diffuse ISM. The mean (weighted by dust mass) starlight heating rate within a pixel is  $\langle U \rangle$ .

Figure 8(a) is a map of  $U_{\min}$  for M31. The  $U_{\min}$  parameter is strongly peaked at the center. Figure 8(b) shows a generally smooth decline of  $U_{\min}$  with increasing galactocentric radius  $R$ , declining from  $U_{\min} \approx 25$  in the central 200 pc (at S350 resolution) to  $U_{\min} \approx 0.2$  at  $R = 16$  kpc. Beyond 16 kpc,  $U_{\min}$  obtained from single-pixel modeling (triangles) begins to differ from  $U_{\min}$  obtained from annular photometry (circles).

For starlight with the interstellar radiation field spectrum of Mathis et al. (1983, hereafter MMP83) the dust heating rate parameter  $U$  is

$$U = \frac{u_{\star}}{8.6 \times 10^{-13} \text{ erg cm}^{-3}} \quad , \quad (12)$$

where  $u_{\star}$  is the starlight energy density. For the DL07 model, the characteristic grain temperature (of the grains dominating the emission at  $\lambda > 100 \mu\text{m}$ ) is related to the heating rate parameter  $U$  as

$$T_{d, \text{char}} \approx 18 U^{1/6} \text{ K} \quad . \quad (13)$$

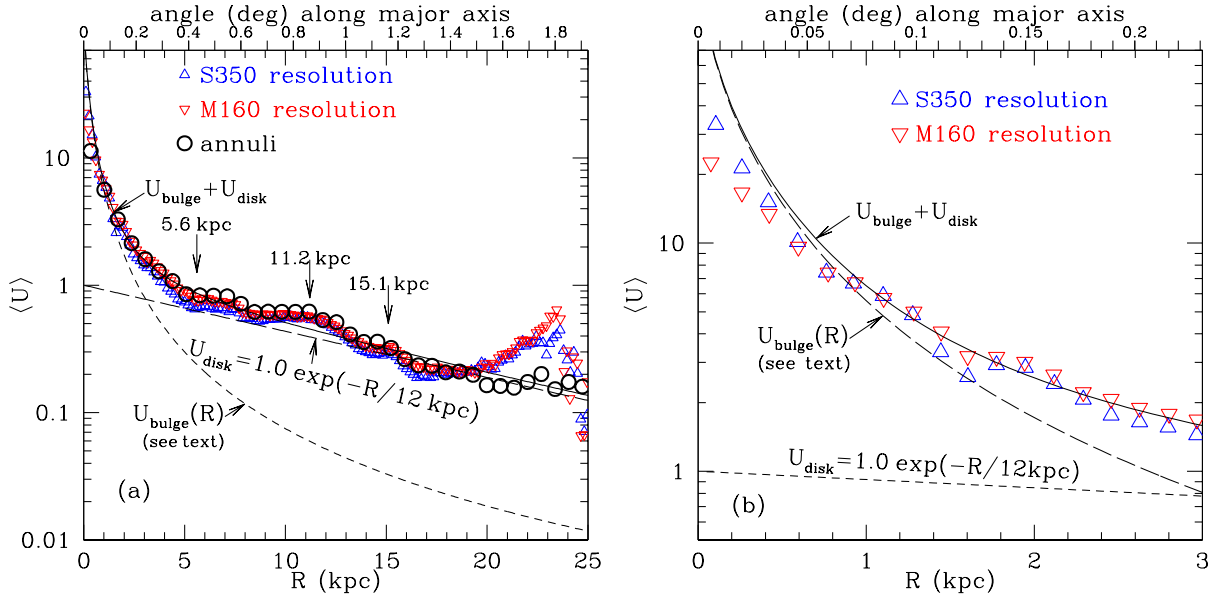


Fig. 10.— (a) Radial profile of  $\langle U \rangle$  in M31 from modeling the IR SED at S350 resolution and at M160 resolution (triangles), and using annular photometry (circles). The dashed curves show the estimated contributions to the heating from disk and bulge stars (see text). (b) Radial profile of  $\langle U \rangle$  in the central 3 kpc.

This is only a representative temperature – dust grains of different sizes and compositions illuminated by a single radiation field have different steady-state temperatures, and very small grains undergo temperature fluctuations due to the quantized heating by stellar photons. Figure 9(b) shows  $T_{\text{d, char}}$  as a function of radius.

The mean starlight heating rate  $\langle U \rangle$  is shown in Figure 9a. At S350 resolution, the center has  $\langle U \rangle \approx 32$  (see Figure 9), corresponding to  $T_{\text{d, char}} \approx 33$  K. At  $R = 15$  kpc we find  $U \approx 0.3$ , or  $T_{\text{d, char}} \approx 15$  K, and at  $R = 20$  kpc we find  $U \approx 0.25$ , or  $T_{\text{d, char}} \approx 14$  K.

Near the center, our  $T_{\text{d, char}} \approx 33$  K is in close agreement with  $T_{\text{d}} \approx 35$  K estimated by Groves et al. (2012), who modeled the  $100 - 500 \mu\text{m}$  SED using a modified blackbody,  $F_{\nu} \propto \nu^2 B_{\nu}(T_{\text{d}})$  in  $\Delta R = 230$  pc annuli for  $0 < R < 15$  kpc. At  $R = 15$  kpc, our  $T_{\text{d, char}} = 15$  K is somewhat higher than the value 12.5 K found by Groves et al. (2012).

How does the starlight heating rate inferred from the dust IR emission compare with what is expected? At  $R > 5$  kpc, the observed mean heating rate  $\langle U \rangle$  in Figure 9(a) is presumably primarily due to starlight from disk stars. In the star-forming parts of the disk, the radiation field heating the dust is from a mixture of young and old stars, modified by dust attenuation;  $\langle U \rangle_{\text{disk}}$  includes the contribution of both young and old stars. Estimating the distribution of  $U$  values seen by the dust would be a challenging radiative transfer problem even if we knew the three-dimensional distributions of stars and dust. The observed  $\langle U \rangle$  in Figure 10(a) shows an

approximately exponential decline with increasing  $R$  out to 20 kpc, which can be approximated by

$$\langle U \rangle_{\text{disk}} \approx 1.0 \exp(-R/12 \text{ kpc}) \quad . \quad (14)$$

This is plotted in Figures 10; we will use it to estimate the contribution of disk starlight to  $\langle U \rangle$  in the central regions.

Near the center of M31, the radiation from the stellar bulge population becomes dominant. The distribution of bulge luminosity, and the resulting energy density of starlight from the bulge, is discussed by Groves et al. (2012), and elaborated further in Appendix B. From a three-dimensional model for the stellar bulge, the energy density of bulge starlight is estimated to be

$$u_{\star, \text{bulge}}^{(0)}(R) = 5.1 \times 10^{-11} I(R/r_b) \text{ erg cm}^{-3} \quad , \quad (15)$$

where  $I(x)$  is given by Equation (B4),  $r_b = 0.58 \text{ kpc}$  is the core radius of the bulge (see Appendix B)<sup>13</sup> and the superscript (0) indicates that it is a theoretical estimate, with dust extinction neglected. For the starlight spectrum of the bulge, we estimate

$$U_{\text{bulge}}^{(0)} = \frac{u_{\star, \text{bulge}}^{(0)}}{1.7 \times 10^{-12} \text{ erg cm}^{-3}} = 30 I(R/r_b) \quad . \quad (16)$$

Equation (16) gives  $U_{\text{bulge}}^{(0)}(R = 1 \text{ kpc}) = 7.9$ , whereas our estimated heating rate from the IR SED at  $R = 1 \text{ kpc}$  is  $\langle U \rangle \approx 7.5$  (see Figure 10), which presumably includes a contribution from disk stars, which is estimated from Equation (14) to be  $\sim 0.92$ . Thus at  $R = 1 \text{ kpc}$  we might estimate the heating contribution of the bulge stars to be  $\sim 6.5$ , 80% of our theoretical estimate  $U_{\text{bulge}}^{(0)}$  at this radius. At smaller radii we find that  $U_{\text{bulge}}^{(0)}$  exceeds the inferred  $\langle U \rangle$  by  $\sim 30\%$ .

There are a number of possible explanations for the discrepancy between the theoretical estimate  $U_{\text{bulge}}^{(0)}$  and  $\langle U \rangle$  estimated from modeling the IR SED: (1) Perhaps the bulge starlight has simply been overestimated by  $\sim 30\%$ . (2) The dust grains that we are using as “photometers” are likely to be mainly located in clouds distributed in a thin disk; internal extinction could lower the starlight heating rate below the optically-thin estimate (Equation 16). (3) Some of the dust is presumably above and below the disk plane; thus the observed emission from the center will include emission from dust that is actually at larger radii, projected onto the center. (4) To estimate  $\langle U \rangle$  from the infrared observations, we have assumed the dust grains to have the properties of dust in the DL07 model. The dust near the center of M31 may well differ from the solar-neighborhood dust on which the DL07 is based. If the dust grains at  $R \lesssim 2 \text{ kpc}$  have a *lower* ratio of (optical absorption cross section)/(FIR absorption cross section) than the DL07 model grains, a given radiation field will heat them to a lower temperature than the DL07 dust. A 30% reduction in the ratio (optical absorption cross section)/(FIR absorption cross section) would be sufficient to remove the

---

<sup>13</sup>Our estimate for  $u_{\star, \text{bulge}}$  (Equation (15)) is slightly below the value  $u_{\star, \text{bulge}}(R) = 5.7 \times 10^{-11} I(R/r_b) \text{ erg cm}^{-3}$  obtained by Groves et al. (2012).



discrepancy. Such a reduction in the ratio of optical absorption to FIR emission cross section would occur if the grain radii in the center were larger by  $\sim 30\%$ .

To approximate our observed heating rate  $\langle U \rangle$ , we will adopt the spatial profile expected for the bulge starlight, but will scale down the heating rate by a factor 0.7. To this we add our empirical estimate (Equation (14)) for the heating due to the disk stars. Thus:

$$\langle U \rangle = U_{\text{bulge}} + \langle U \rangle_{\text{disk}} \quad (17)$$

$$U_{\text{bulge}} = 0.7U_{\text{bulge}}^{(0)} = 21 I(R/r_b) \quad , \quad r_b = 0.58 \text{ kpc} \quad (18)$$

$$\langle U \rangle_{\text{disk}} \approx 1.0 \exp(-R/12 \text{ kpc}) \quad . \quad (19)$$

This estimate of  $U$  is plotted in Figures 9 and 10. The agreement is good, except at  $R < 0.4 \text{ kpc}$  (see Figure 10) where the observed dust heating rates fall somewhat below Equation (17). The deviation at  $R < 0.4 \text{ kpc}$  is likely due to the limited spatial resolution of the observations. Even at S350 resolution, the FWHM of the PSF corresponds to  $\Delta R = 0.4 \text{ kpc}$  along the minor axis. In addition, as already noted above, out-of-plane dust, projected along the line-of-sight, can also act to lower the “observed” dust temperatures near the center.

Using modified blackbody fits, Groves et al. (2012) found dust temperatures in the center that are  $\sim 15\%$  lower than the  $T_{\text{d, char}}$  values found here. Their lower dust temperature estimates may be due to use of an earlier version of the data reduction pipeline and calibration factors, and possibly also to use of a modified blackbody rather than the multicomponent physical grain model used here.

To summarize, we find relatively good agreement between the observed dust emission spectrum and that which would be expected for heating by a combination of the bulge starlight and a disk heating component. The observed dust temperatures are only slightly below what would be expected. The inferred heating rate from the bulge stars is only  $\sim 30\%$  lower than predicted for a simple model of the bulge starlight. The 30% discrepancy in heating rate corresponds to only a 5% discrepancy in grain temperature. Given that there are a number of effects that could account for such a discrepancy, this agreement is gratifying.

The dust temperature  $T$  depends on the starlight heating rate parameter  $U$  and on the ratio  $\langle C_{\text{abs}} \rangle_{\star}(a) / \langle C_{\text{abs}} \rangle_T(a)$ , where  $\langle C_{\text{abs}} \rangle_{\star}(a)$  is the dust absorption cross section averaged over the spectrum of the illuminating starlight for a grain of radius  $a$ , and  $\langle C_{\text{abs}} \rangle_T(a)$  is the Planck-averaged absorption cross section for grain temperature  $T$ . The fact that the observed dust temperature is within 5% of the predicted dust temperature indicates that the actual values of  $\langle C_{\text{abs}} \rangle_{\star} / \langle C_{\text{abs}} \rangle_T$  are close to the values in the DL07 grain model. This builds confidence in our grain model, and hence in the dust mass estimates, which are proportional to  $\rho a / \langle C_{\text{abs}} \rangle_T(a)$ . Given the extreme environmental differences, it is remarkable that the dust properties near the center of M31 appear to be so similar to values inferred for dust in the solar neighborhood.

## 8. PAH Abundance

The intensity in the IRAC bands includes both direct starlight and emission from dust population. The observed intensities at  $\lambda \geq 3.6\mu\text{m}$  are modeled as the sum of a stellar component (modeled as a 5000K blackbody) plus a nonstellar component  $(F_\nu)_{\text{ns}}$  contributed primarily by PAHs. In practice, the stellar component is determined by the IRAC3.6 and IRAC4.5 photometry; subtraction of the stellar component typically leaves a positive “nonstellar” residual in IRAC5.8 and IRAC8.0 that can be reproduced by varying the PAH abundance in the dust model.

The parameter  $q_{\text{PAH}}$  in the DL07 model is defined to be the fraction of the total dust mass contributed by PAHs containing fewer than  $10^3$  C atoms. In the model fitting,  $q_{\text{PAH}}$  is essentially proportional to the ratio of the power in the 6.2 and  $7.7\mu\text{m}$  PAH emission features divided by the total power radiated by the dust. When only IRAC photometry is available for  $\lambda < 20\mu\text{m}$ , the  $q_{\text{PAH}}$  parameter is, in practice, proportional to the nonstellar contribution to IRAC8.0 divided by the aggregate 70– $350\mu\text{m}$  luminosity. For a fixed starlight spectrum,  $F(8\mu\text{m})$  is approximately proportional to  $q_{\text{PAH}}$  and to the total infrared power,  $F_{\text{TIR}}$ :

$$(\nu F_\nu)_{\text{IRAC8,ns}} \approx A_\star q_{\text{PAH}} F_{\text{TIR}} \quad , \quad (20)$$

where  $(\nu F_\nu)_{\text{IRAC8,ns}}$  is the non-stellar contribution to the IRAC 8.0 $\mu\text{m}$  band, and the dimensionless coefficient  $A_\star$  depends on the spectrum of the illuminating starlight. Draine & Li (2007) show that  $A_{\text{MMP83}} \approx 4.72$  for the MMP83 spectrum of the starlight in the solar neighborhood.

Varying the spectrum of the starlight can cause  $A_\star$  to change, for two reasons. (1) The PAH absorption cross section depends on wavelength differently from the absorption of overall grain mixture ( $\propto F_{\text{TIR}}$ ), hence the fraction of the starlight power that is absorbed by PAHs will depend on the spectrum. (2) The PAH emission spectrum is the result of single-photon heating, hence the fraction of energy absorbed by PAHs that is reradiated in the IRAC8.0 band depends on the illuminating spectrum. As an example of the dependence of  $A_\star$  on the illuminating spectrum, Draine (2011a) showed that  $A_{20\text{kK}} \approx 7.1 = 1.5A_{\text{MMP83}}$  for a 20kK blackbody cut off at 13.6 eV.

Draine & Li (2014, in preparation) calculated the emission from the DL07 dust model for illumination by starlight with the spectrum of the M31 bulge population, finding  $A_{\text{bulge}} \approx 1.95$ . For a mixed spectrum, where the overall dust heating rate is  $U = U_{\text{bulge}} + U_{\text{MMP83}}$ , the effective value is the dust luminosity-weighted mean

$$A_\star = \frac{A_{\text{bulge}}U_{\text{bulge}} + A_{\text{MMP83}}U_{\text{MMP83}}}{U_{\text{bulge}} + U_{\text{MMP83}}} = \frac{1.95U_{\text{bulge}} + 4.72U_{\text{MMP83}}}{U_{\text{bulge}} + U_{\text{MMP83}}} \quad . \quad (21)$$

To correct the estimate of  $q_{\text{PAH}}$  made assuming the MMP83 radiation field, we will take

$$(q_{\text{PAH}})_{\text{corr}} = \frac{4.72}{A_\star} \times (q_{\text{PAH}})_{\text{MMP83}} \quad (22)$$

where  $(q_{\text{PAH}})_{\text{MMP83}}$  is the value of  $q_{\text{PAH}}$  estimated assuming the dust to be heated by starlight with the MMP83 spectrum, with  $U_{\text{bulge}}$  and  $U_{\text{MMP83}}$  given by Equations (18) and (19).

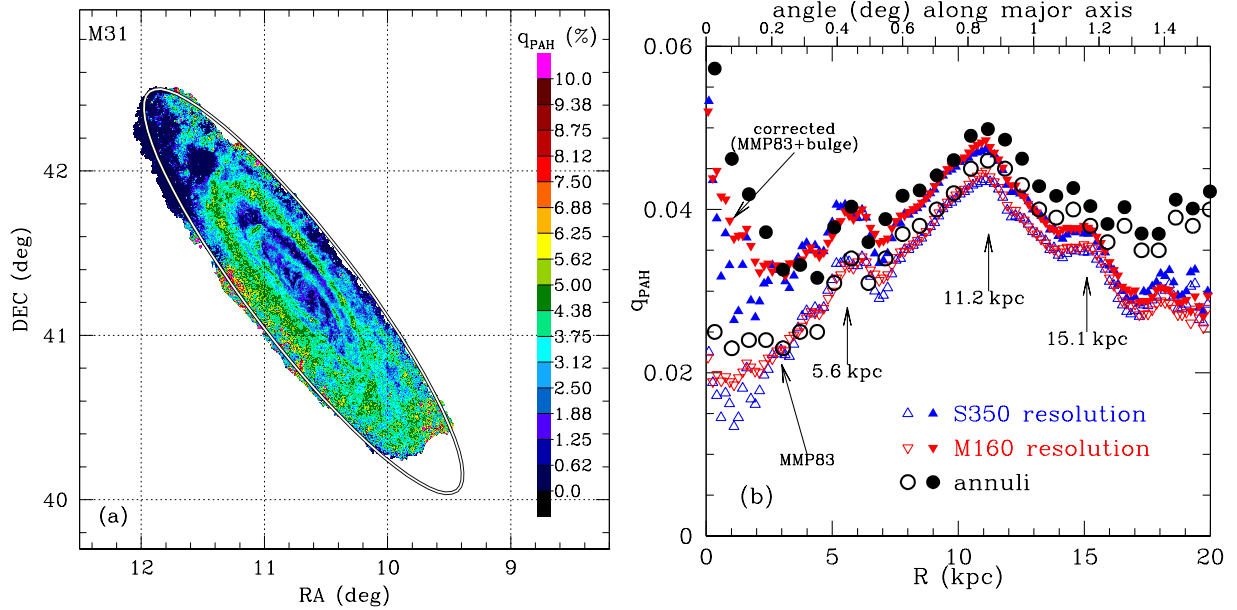


Fig. 11.— (a) Map of PAH abundance parameter  $(q_{\text{PAH}})_{\text{MMP83}}$  in M31 at S350 resolution. The low values of  $q_{\text{PAH}}$  in the NE may be due to problems with background subtraction in IRAC5.8 and IRAC8.0 (see text). (b) Radial profiles:  $(q_{\text{PAH}})_{\text{MMP83}}$  (open symbols) and  $(q_{\text{PAH}})_{\text{corr}}$  from Equation (22) (filled symbols).

A map of  $(q_{\text{PAH}})_{\text{MMP83}}$  at S350 resolution is shown in Figure 11(a). Figure 11(b) shows the radial profile of  $(q_{\text{PAH}})_{\text{MMP83}}$  and  $(q_{\text{PAH}})_{\text{corr}}$ . Interestingly,  $q_{\text{PAH}}$  appears to peak in the 11 kpc ring, attaining a value  $(q_{\text{PAH}})_{\text{corr}} \approx 0.049$  that is close to the value  $q_{\text{PAH}} \approx 0.045$  estimated for the diffuse ISM in the solar neighborhood.

In Figure 11,  $(q_{\text{PAH}})_{\text{MMP83}}$  declines as one approaches the center, reaching a value  $(q_{\text{PAH}})_{\text{MMP83}} \approx 0.02$  in the central regions. However, this decline is largely an artifact of assuming that the spectrum of the illuminating starlight is independent of radius, which is incorrect – in the central regions the starlight is dominated by light from the bulge stars, which is much redder than the MMP83 spectrum.

Figure 11(b) shows that when we allow for the starlight being increasingly dominated by an old stellar population as we move to the center,  $(q_{\text{PAH}})_{\text{corr}}$  shows only limited variation as we move from  $R = 11$  kpc to the central kpc. Evidently the balance between PAH formation and destruction in the ISM remains relatively constant from the central kpc out to  $R = 20$  kpc. There does appear to be a systematic radial decline in  $q_{\text{PAH}}$  for  $R > 11$  kpc, but this again might be an artifact of a radial gradient in the spectrum of the starlight as one moves from the 11.2 kpc ring – where star formation is active – to outer regions where there appears to be little contemporary star formation.

At  $R \gtrsim 20$  kpc  $q_{\text{PAH}}$  estimated from the  $\Delta R = 677$  pc annuli appears to rise. However, we suspect this to be an artifact of imperfect background subtraction in the 5.8 and 8.0  $\mu\text{m}$  images.

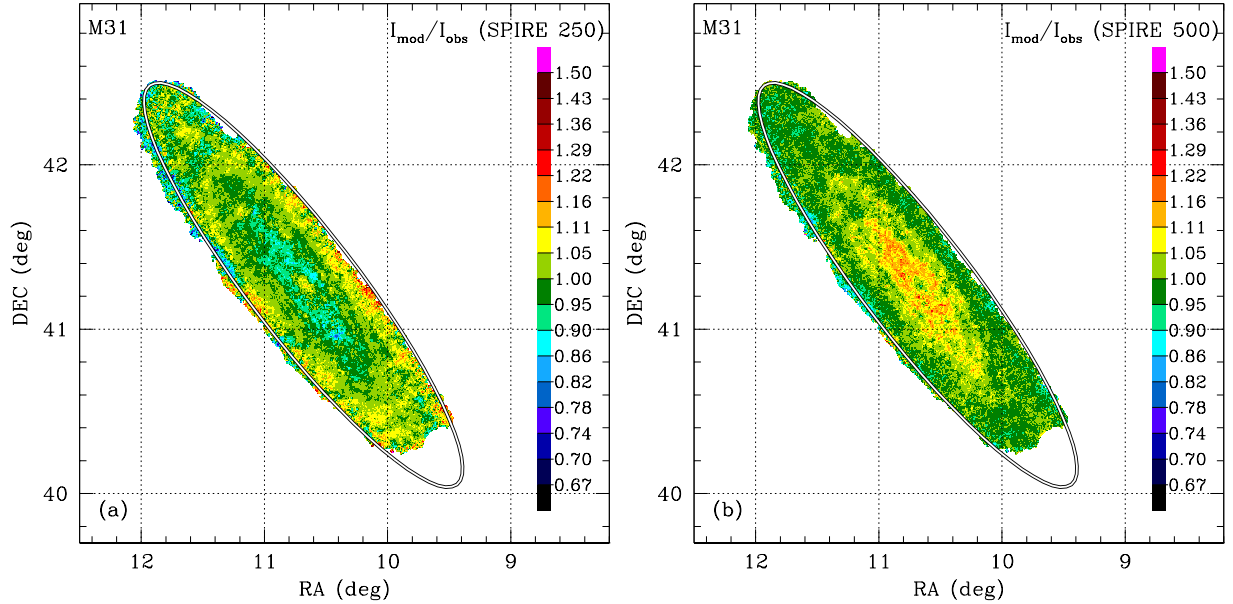


Fig. 12.— For M160 resolution modeling: ratio of the model intensity divided by the observed intensity for the SPIRE 250 and 500 $\mu\text{m}$  bands. The DL07 model successfully fits the 500 $\mu\text{m}$  emission out to the edge of the “galaxy mask”, at  $R \approx 20$  kpc. In the inner regions, the DL07 model tends to underpredict SPIRE 250 $\mu\text{m}$  and overpredict SPIRE 500 $\mu\text{m}$  (see also Figure 13), but the deviations are only at the  $\sim 10\%$  level.

Although background subtraction works well in other bands out to  $\sim 25$  kpc, it appears less successful for the IRAC 5.8 $\mu\text{m}$  and 8.0 $\mu\text{m}$  bands. The difficulty with background subtraction may be due to systematic effects on the IRAC detectors, including an effect referred to as “banding”, multiplexor “bleeding”, and scattered light (Hora et al. 2004). The SAGE-SMC survey (Gordon et al. 2011) was able to minimize these problems by combining images taken with very different roll angles together with custom processing techniques, but we are simply using the M31 images from Barmby et al. (2006). It is also possible that the Galactic foreground has structure arising from variations in PAH abundance or ionization state on  $\sim 0.5^\circ$  scales, which would not be identified by the background subtraction procedures used here.

## 9. Dust Properties

In the present work, we attempt to reproduce the observed SED in each pixel using the DL07 dust model and a parameterized distribution of starlight intensities. Above we have examined the values of the dust modeling parameters, such as the dust mass,  $q_{\text{PAH}}$ , and properties of the starlight intensity distribution. Here we compare the models with observations to see how well the model actually reproduces the data, and whether any systematic deviations are present that indicate systematic problems with the modeling.

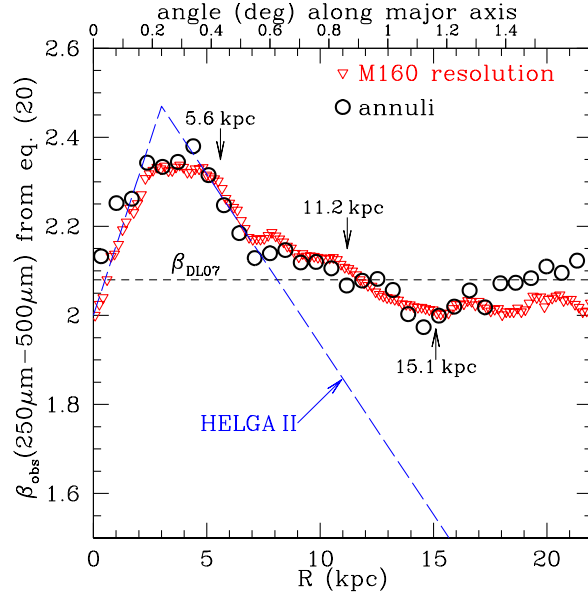


Fig. 13.— Opacity spectral index  $\beta_{\text{obs}}$  from Equation (23) obtained from modeling at M160 resolution (triangles) and using annular photometry (circles). The DL07 model overpredicts the SPIRE500/SPIRE250 band ratio by a factor  $> 1.2$  between  $R \approx 2$  kpc and  $R \approx 6$  kpc, corresponding to  $\beta_{\text{obs}} > \beta_{\text{DL07}} + 0.26$ . For  $R \gtrsim 10$  kpc the DL07 model agrees with the observations to within 10%, and the model appears to have nearly the correct value of  $\beta$ . Also shown is the HELGA II (Smith et al. 2012) result for  $\beta$  (see text).

Aside from minor effects associated with variation in the PAH abundance when  $q_{\text{PAH}}$  is allowed to vary, the composition (amorphous silicate and graphitic carbon) is assumed to be the same everywhere in the DL07 models used to fit the infrared emission. Further, the dust opacity is assumed to be independent of temperature. The DL07 dust model used here has an opacity with a fixed dependence on frequency at long wavelengths ( $\lambda \gtrsim 50 \mu\text{m}$ ). Here we compare the model to the observed emission from M31 to look for residuals that might be indicative of differences between the model and the actual dust in M31.

We will focus on the behavior of the dust opacity in the 250–500  $\mu\text{m}$  region. Figure 12 shows the ratio of model to observation at SPIRE250 and SPIRE500. The first impression is that the model is good: the ratio of model to observation is generally between 0.86 and 1.16, which seems good in view of noise in the observations, uncertainties in calibration, and the general uncertainties in the adopted dust opacities. However, systematic trends are evident: in the central regions of M31 (excluding the center itself) the model tends to be low at SPIRE250, and high at SPIRE500.

Let  $\beta \equiv \ln[\kappa(250 \mu\text{m})/\kappa(500 \mu\text{m})]/\ln 2$  be the effective power-law index of the dust opacity between 250 and 500  $\mu\text{m}$ . For the DL07 model (see Table 2) this ratio is  $\beta_{\text{DL07}} = 2.08$ . If the fitted dust temperatures were left unchanged, the 500/250 flux ratio could be brought into agreement

with observations if  $\beta$  were changed to

$$\beta_{\text{obs}} = \beta_{\text{DL07}} + \frac{\ln([I_{\nu}(250\mu\text{m})/I_{\nu}(500\mu\text{m})]_{\text{obs}}/[I_{\nu}(250\mu\text{m})/I_{\nu}(500\mu\text{m})]_{\text{model}})}{\ln(500/250)} . \quad (23)$$

Figure 13 shows  $\beta_{\text{obs}}$  as a function of  $R$  for  $R < 22$  kpc, using only M160 resolution pixels with  $\Sigma_{Ld} > \Sigma_{Ld,\text{min}}$ . For  $1 < R < 10$  kpc,  $\beta_{\text{obs}}$  is larger than  $\beta_{\text{DL07}}$ , indicating that the opacity between 250 and  $500\mu\text{m}$  should fall more rapidly than  $\nu^{2.08}$ .

The dust opacity ratio  $\kappa(250\mu\text{m})/\kappa(500\mu\text{m})$  could vary with location because the dust composition is varying, or it could conceivably result from variations of the grain temperature, if the dust opacities are temperature-dependent. The DL07 model assumes the dust opacities to be independent of temperature. However, some materials do exhibit temperature-dependent opacities in the laboratory (e.g., Mennella et al. 1998; Boudet et al. 2005; Coupeaud et al. 2011), and such behavior is expected in some models of amorphous solids (Meny et al. 2007). A number of studies have claimed that interstellar dust opacities are temperature-dependent (Dupac et al. 2003; Paradis et al. 2010, 2011; Liang et al. 2012) although apparent  $\beta - T$  correlations can arise from both observational noise and line-of-sight temperature variations (Shetty et al. 2009a,b; Kelly et al. 2012). The “two level system” (TLS) model (Meny et al. 2007; Paradis et al. 2011) predicts that increasing dust temperature  $T$  should lead to a *lower* value of  $\beta$ . However, in M31 it appears that the 1–10 kpc regions where the dust is warmer than the outer disk have a *larger* value of  $\beta$  than the value in the outer disk, and the center – where the dust is hottest – has essentially the same value of  $\beta$  as the relatively cold dust at  $R \approx 20$  kpc. The observed variations in  $\beta$  do not seem to be consistent with what would be expected for the TLS model, unless one allows for substantial radial variations in the TLS model parameters themselves. Rather than attributing the apparent changes in  $\beta$  to temperature, it would appear instead that the dust composition must be varying with radius in M31.

The HELGA II collaboration (Smith et al. 2012) reported a sharp change in the dust properties at  $R \approx 3$  kpc, based on the value of the dust emissivity index  $\beta$  obtained from their modified blackbody fits. Interior to 3 kpc, the inferred dust temperature decreased from  $T = 27.5$  K at the center to  $T = 16.8$  K at  $R = 3.0$  kpc, with  $\beta$  simultaneously rising from 2 to 2.5; beyond  $R = 3$  kpc, they found the temperature to be rising and  $\beta$  falling with increasing  $R$ , reaching  $T = 18$  K and  $\beta = 1.5$  at  $R = 15$  kpc. The decrease in  $\beta$  at large  $R$  was invoked to account for an apparent “ $500\mu\text{m}$  excess”.

The HELGA II result for  $\beta$ , shown in Figure 13, is similar to the present study for  $R \lesssim 7$  kpc, but we find very different behavior for  $R \gtrsim 7$  kpc. We see no evidence of a  $500\mu\text{m}$  excess at large  $R$  – quite the contrary, the DL07 model tends to slightly *overpredict* SPIRE500 in the outer regions of M31.

The HELGA II analysis was based on observations of M31 that were shallower than the data used here, and also used an earlier calibration of the three SPIRE bands. It is possible that the differences between the HELGA II results and those of the present study may be due in part to

differences in signal/noise, calibration or data reduction pipeline. In the outer regions results are also sensitive to background subtraction.

If we were over- or under-subtracting the IR backgrounds, we would obtain very low or very high dust/gas ratios. The fact that we obtain sensibly-behaved dust/H ratios out to  $R = 25$  kpc (see Figures 6 and 7) is evidence that the automatic background subtraction algorithm used here (Aniano et al. 2012) – which is based only on the IR imaging, and makes no use of H I 21 cm or CO emission – is working well, at least out to  $R = 25$  kpc.

Our overall conclusion is that the DL07 dust properties appear to provide a generally good match to the observations of M31, except for the need for a modest increase in the opacity index  $\beta$  in the 2–6 kpc region. It would be of interest to apply this same approach to other galaxies (e.g., M33) to see if similar variations in  $\beta_{\text{obs}}$  are found.

## 10. Summary

The principal conclusions of this work are as follows:

1. Consistent with previous observations, we find that the dust mass surface density in M31 peaks in two rings, at  $R = 5.6$  kpc and  $R = 11.2$  kpc, with a third ring seen at  $R \approx 15.1$  kpc.
2. We find a total dust mass  $M_d = (5.4 \pm 1.1) \times 10^7 M_\odot$  within  $R = 25$  kpc. 95% of this dust mass lies within  $R = 21$  kpc, with the dust surface density peaking at  $R = 11.2$  kpc.
3. The dust/H mass ratio exhibits a smooth radial decline with increasing  $R$ , from  $\sim 0.027$  at the center to  $\sim 0.0027$  at  $R = 25$  kpc.
4. The dust/H mass ratio parallels measurements of O/H in H II regions, consistent with a constant fraction of the refractory elements Mg, Si, and Fe being in dust. Based on our estimated dust/H mass ratio, we infer that the metallicity  $Z/Z_\odot$  varies from  $\sim 3$  at  $R = 0$  to  $\sim 0.3$  at  $R = 25$  kpc – see Figure 7(b) and Equation (10).
5. The starlight heating rate parameter  $\langle U \rangle$  shows a nearly monotonic decline with galactocentric radius, from  $\langle U \rangle \approx 50$  at the center (at S350 resolution) to  $\langle U \rangle \approx 0.2$  at  $R \approx 20$  kpc.
6. We confirm the finding of Groves et al. (2012) that the dust heating in the central 2 kpc is dominated by light from the stellar bulge. We find that the starlight heating rates inferred from the observed IR emission are consistent with the heating rates expected from the bulge starlight. It is remarkable that the dust properties near the center of M31 appear to be similar to the properties of dust in the solar neighborhood.
7. After taking into account variation in the spectrum of the starlight, we find the PAH abundance  $q_{\text{PAH}}$  to be approximately constant from the center of M31 out to  $\sim 20$  kpc. There is

some indication of decline with  $R$  for  $R > 11$  kpc. The global value of  $q_{\text{PAH}} = 0.039$  for  $R < 17$  kpc.

8. While the DL07 dust model generally provides a good fit to the observed SED, there are some systematic deviations. The dust at  $R \approx 1 - 6$  kpc appears to have an opacity spectral index  $2.2 < \beta < 2.33$  in the 250–500 $\mu\text{m}$  wavelength range, whereas the dust at  $R > 7$  kpc has  $\beta \approx 2.08$ , consistent with the dust in the DL07 model. We are in approximate agreement with the radial variation of  $\beta$  found by HELGA II (Smith et al. 2012) in the central  $\sim 7$  kpc, but do not confirm their finding of low  $\beta$  values for  $R > 8$  kpc.
9. At large radii  $R \gtrsim 10$  kpc the DL07 model, with fixed opacity, is consistent with the observed photometry, and returns dust masses that are consistent with the observations of the gas and metallicity.

We thank Edvige Corbelli, Stephen Eales, Jeremy Goodman, Matthew Smith, and the anonymous referee for helpful comments. This work was supported in part by NSF grant AST 1008570. G.A. acknowledges support from European Research Council grant ERC-267934.

### A. PACS versus MIPS

MIPS and PACS have two wavelengths in common: 70 $\mu\text{m}$  and 160 $\mu\text{m}$ . While the filter response functions are not identical, they are similar enough that we would expect MIPS and PACS to measure very similar flux densities for smooth SEDs. However, comparisons of MIPS and PACS imaging often shows discrepancies that are much larger than expected – see, e.g., the cases of NGC 628 and NGC 6946 (Aniano et al. 2012).

Figure 14 shows the ratio of PACS/MIPS photometry of M31 in the 70 and 160 $\mu\text{m}$  bands, after first convolving each image to the common resolution of the MIPS160 PSF.

The PACS70/MIPS70 comparison is particularly striking: while there are a few regions near the center with PACS70/MIPS70  $\sim 0.7$ , many regions have PACS70/MIPS70  $> 2$ . The fact that this occurs over extended regions makes it clear that this is not simply a consequence of random noise. The fact that it is non-uniform over the image makes it clear that it is not simply a result of calibration. Background subtraction is of critical importance, but we have employed the same background estimation procedures (Aniano et al. 2012) for both MIPS and PACS. It is now thought that MIPS70 suffers from sub-linear behavior in high-surface brightness regions, but such high surface brightnesses are found only at the center of M31, whereas we see high values of PACS70/MIPS70 occurring across the disk. The reason for the photometric discrepancy is unclear, and we therefore opt to use both MIPS70 and PACS70 data in our model-fitting.

The PACS160/MIPS160 comparison is much more satisfactory than the PACS70/MIPS70 comparison, but there are still many regions – particularly along the 11 kpc ring – where PACS160/MIPS160



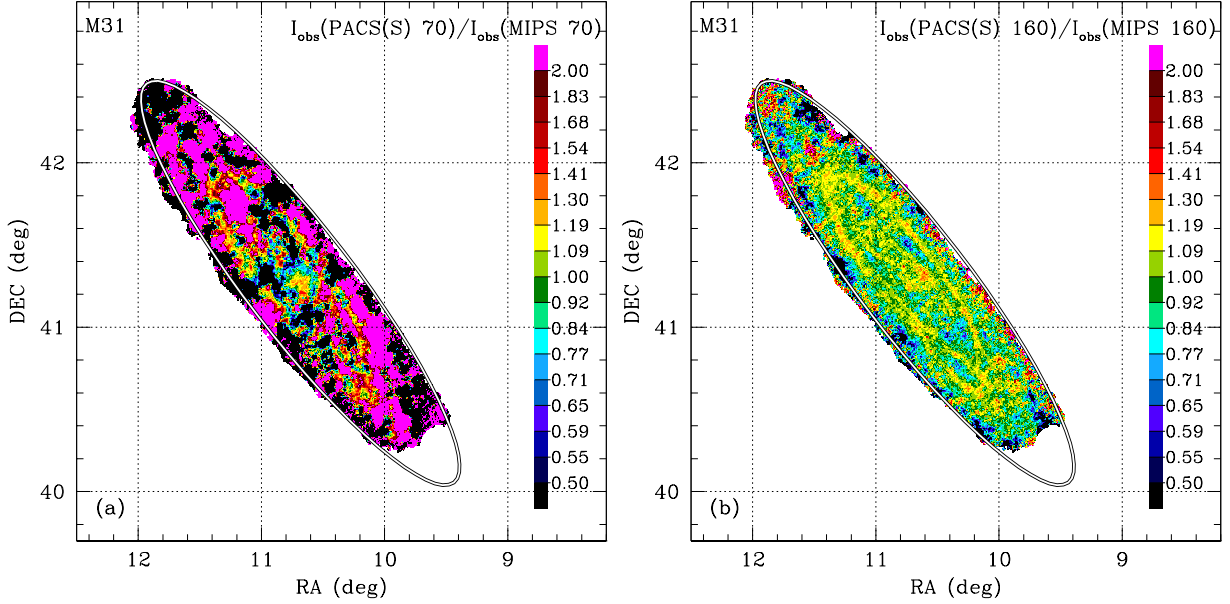


Fig. 14.— Ratios of images convolved to the MIPS160 PSF, displayed within the “galaxy mask” where the signal/noise is high enough that dust modeling is possible. Left: ratio of PACS70/MIPS70. Right: ratio of PACS160/MIPS160.

$> 1.4$ . This difference is much larger than the claimed uncertainties in the observed intensities at these locations. MIPS160 is now thought to have sublinear response for  $I_\nu \gtrsim 50 \text{ MJy sr}^{-1}$  (Paladini et al. 2012), but most of M31 is below this value. This again emphasizes the value of being able to include the MIPS160 data in the analysis, possible only if one degrades all the other imaging to the MIPS160 PSF (FWHM  $39''$ ).

## B. Heating by Bulge Starlight

Groves et al. (2012) have discussed the contribution of M31’s bulge stars to the heating of dust. For the adopted bulge stellar luminosity density profile (Geehan et al. 2006)

$$\rho_\star(R) = \frac{L_{\text{bulge}}}{2\pi r_b^3} \frac{1}{(R/r_b)(1 + R/r_b)^3} \quad , \quad (\text{B1})$$

the starlight energy density due to bulge stars (neglecting possible absorption or scattering by dust)

is

$$u_{\star, \text{bulge}}(R) = \frac{L_{\text{bulge}}}{4\pi r_b^2 c} I(R/r_b) \quad (\text{B2})$$

$$I(x) \equiv \frac{1}{x} \int_0^\infty \frac{\ln\left(\frac{x+y}{|x-y|}\right)}{(1+y)^3} dy \quad (\text{B3})$$

$$= \frac{1}{x^2 - 1} + \frac{\ln(1+x)}{2x(1+x)^2} - \frac{2 \ln x}{(x^2 - 1)^2} \quad (\text{B4})$$

$I(x)$  is logarithmically divergent for  $x \rightarrow 0$ . Near  $x = 1$ ,

$$I(x = 1 + \epsilon) = \frac{1}{2} + \frac{\ln 2}{8} - 0.778(x - 1) + O((x - 1)^2) \quad (\text{B5})$$

The projected luminosity interior to radius  $R$  is

$$L(< R) = \int_0^R \rho_\star(r) 4\pi r^2 dr + \int_R^\infty \rho_\star(r) \left[1 - \sqrt{1 - (R/r)^2}\right] 4\pi r^2 dr \quad (\text{B6})$$

$$= L_{\text{bulge}} \left[1 - 2\alpha \int_0^{\pi/2} \frac{\cos^2 \theta d\theta}{(1 + \alpha \sin \theta)^3}\right] \quad \alpha \equiv \frac{r_b}{R} \quad (\text{B7})$$

$$= 0.4711 L_{\text{bulge}} \quad \text{for } \alpha = 0.61 \quad (\text{B8})$$

We obtain  $L_{\text{bulge}}$  by integrating the average of the intrinsic and reddened spectrum obtained by Groves et al. (2012) for  $L(< 1 \text{ kpc})$  over the wavelength interval  $[0.0912 \mu\text{m}, 4 \mu\text{m}]$ . Groves et al. (2012) assumed  $D = 780 \text{ kpc}$  and  $r_b = 0.61 \text{ kpc}$ . Corrected to  $D = 744 \text{ kpc}$ , we obtain  $L_{\text{bulge}}(0.0912 - 4 \mu\text{m}) = 1.60 \times 10^{10} L_\odot$ , with  $r_b = 0.58 \text{ kpc}$ . Thus, the  $0.0912 \mu\text{m} < \lambda < 4 \mu\text{m}$  energy density due to the bulge stars is

$$u_{\star, \text{bulge}}(R) = 5.07 \times 10^{-11} I(R/r_b) \text{ erg cm}^{-3} \quad (\text{B9})$$

This energy density of bulge starlight gives a theoretical estimate for the dust heating rate, normalized to the heating rate for the MMP83 radiation field,

$$U_{\text{bulge}}^{(0)}(R) = 30 I(R/r_b) \quad (\text{B10})$$

For  $R = 1 \text{ kpc}$  this gives  $U_{\text{bulge}}^{(0)}(1 \text{ kpc}) = 7.9$ . This is our zero-th order estimate for the dust heating rate in the central few kpc of M31. In Section 7 we show that this theoretical estimate for the dust heating rate agrees well with the dust heating rate inferred from the IR SED.

## REFERENCES

Aniano, G., Draine, B. T., Calzetti, D., et al. 2012, ApJ, 756, 46

Aniano, G., Draine, B. T., Gordon, K. D., & Sandstrom, K. M. 2011, PASP, 123, 1218

- Barmby, P., Ashby, M. L. N., Bianchi, L., et al. 2006, *ApJ*, 650, L45
- Block, D. L., Bournaud, F., Combes, F., et al. 2006, *Nature*, 443, 832
- Bogdán, Á., & Gilfanov, M. 2008, *MNRAS*, 388, 56
- Bolatto, A. D., Wolfire, M., & Leroy, A. K. 2013, *ARA&A*, 51, 207
- Boudet, N., Mutschke, H., Nayral, C., et al. 2005, *ApJ*, 633, 272
- Braun, R., Thilker, D. A., Walterbos, R. A. M., & Corbelli, E. 2009, *ApJ*, 695, 937
- Chemin, L., Carignan, C., & Foster, T. 2009, *ApJ*, 705, 1395
- Ciardullo, R., Rubin, V. C., Jacoby, G. H., Ford, H. C., & Ford, W. K., Jr. 1988, *AJ*, 95, 438
- Corbelli, E., Lorenzoni, S., Walterbos, R., Braun, R., & Thilker, D. 2010, *A&A*, 511, A89
- Coupeaud, A., Demyk, K., Meny, C., et al. 2011, *A&A*, 535, A124
- Crane, P. C., Dickel, J. R., & Cowan, J. J. 1992, *ApJ*, 390, L9
- Dalcanton, J. J., Williams, B. F., Lang, D., et al. 2012, *ApJS*, 200, 18
- de Vaucouleurs, G., de Vaucouleurs, A., Corwin, H. G., Jr., et al. 1991, *Third Reference Catalogue of Bright Galaxies* (New York: Springer)
- Devereux, N. A., Price, R., Wells, L. A., & Duric, N. 1994, *AJ*, 108, 1667
- Draine, B. T. 2003, *ARA&A*, 41, 241
- Draine, B. T. 2011a, in *EAS Publications Series*, Vol. 46, *PAHs and the Universe*, ed. C. Joblin & A. G. G. M. Tielens, 29
- Draine, B. T. 2011b, *Physics of the Interstellar and Intergalactic Medium* (Princeton, NJ: Princeton Univ. Press)
- Draine, B. T., Dale, D. A., Bendo, G., et al. 2007, *ApJ*, 663, 866
- Draine, B. T., & Li, A. 2001, *ApJ*, 551, 807
- Draine, B. T., & Li, A. 2007, *ApJ*, 657, 810
- Dupac, X., Bernard, J.-P., Boudet, N., et al. 2003, *A&A*, 404, L11
- Fazio, G. G., Hora, J. L., Allen, L. E., et al. 2004, *ApJS*, 154, 10
- Fritz, J., Gentile, G., Smith, M. W. L., et al. 2012, *A&A*, 546, A34
- Geehan, J. J., Fardal, M. A., Babul, A., & Guhathakurta, P. 2006, *MNRAS*, 366, 996

- Gordon, K. D., Bailin, J., Engelbracht, C. W., et al. 2006, *ApJ*, 638, L87
- Gordon, K. D., Meixner, M., Meade, M. R., et al. 2011, *AJ*, 142, 102
- Griffin, M. J., Abergel, A., Abreu, A., et al. 2010, *A&A*, 518, L3
- Griffin, M. J., North, C. E., Schulz, B., et al. 2013, *MNRAS*, 1306.1778
- Groves, B., Krause, O., Sandstrom, K., et al. 2012, *MNRAS*, 426, 892
- Haas, M., Lemke, D., Stickel, M., et al. 1998, *A&A*, 338, L33
- Habing, H. J., Miley, G., Young, E., et al. 1984, *ApJ*, 278, L59
- Hora, J. L., Fazio, G. G., Allen, L. E., et al. 2004, in *Society of Photo-Optical Instrumentation Engineers (SPIE) Conference Series*, Vol. 5487, 77
- Kelly, B. C., Shetty, R., Stutz, A. M., et al. 2012, *ApJ*, 752, 55
- Kennicutt, R. C., Calzetti, D., Aniano, G., et al. 2011, *PASP*, 123, 1347
- Leroy, A. K., Bolatto, A., Gordon, K., et al. 2011, *ApJ*, 737, 12
- Lewis, G. F., Braun, R., McConnachie, A. W., et al. 2013, *ApJ*, 763, 4
- Li, A., & Draine, B. T. 2001, *ApJ*, 554, 778
- Liang, Z., Fixsen, D. J., & Gold, B. 2012, submitted to *MNRAS*(arXiv:1201.0060)
- Mathis, J. S., Mezger, P. G., & Panagia, N. 1983, *A&A*, 128, 212
- Mennella, V., Brucato, J. R., Colangeli, L., et al. 1998, *ApJ*, 496, 1058
- Meny, C., Gromov, V., Boudet, N., et al. 2007, *A&A*, 468, 171
- Neugent, K. F., Massey, P., & Georgy, C. 2012, *ApJ*, 759, 11
- Nieten, C., Neininger, N., Guélin, M., et al. 2006, *A&A*, 453, 459
- Paladini, R., Linz, H., Altieri, B., & Ali, B. 2012, PACS ICC Document, PICC-NHSC-TR-034
- Paradis, D., Bernard, J. P., Mény, C., & Gromov, V. 2011, *A&A*, 534, A118
- Paradis, D., Veneziani, M., Noriega-Crespo, A., et al. 2010, *A&A*, 520, L8
- Pilbratt, G. L., Riedinger, J. R., Passvogel, T., et al. 2010, *A&A*, 518, L1
- Planck Collaboration, Ade, P. A. R., Aghanim, N., et al. 2013a, *ArXiv e-prints*, 1307.6815
- Planck Collaboration, Ade, P. A. R., Aghanim, N., et al. 2013b, *arXiv:1303.5062*, 1303.5062

- Planck Collaboration, Ade, P. A. R., Aghanim, N., et al. 2013c, ArXiv e-prints, 1303.5072
- Planck Collaboration, Ade, P. A. R., Aghanim, N., et al. 2011, A&A, 536, A19
- Poglitsch, A., Waelkens, C., Geis, N., et al. 2010, A&A, 518, L2
- Popescu, C. C., & Tuffs, R. J. 2013, ArXiv e-prints, 1305.0232
- Reach, W. T., Megeath, S. T., Cohen, M., et al. 2005, PASP, 117, 978
- Rieke, G. H., Young, E. T., Engelbracht, C. W., et al. 2004, ApJS, 154, 25
- Roussel, H. 2013, PASP, 125, 1126
- Shetty, R., Kauffmann, J., Schnee, S., & Goodman, A. A. 2009a, ApJ, 696, 676
- Shetty, R., Kauffmann, J., Schnee, S., Goodman, A. A., & Ercolano, B. 2009b, ApJ, 696, 2234
- Smith, M. W. L., Eales, S. A., Gomez, H. L., et al. 2012, ApJ, 756, 40
- Tabatabaei, F. S., & Berkhuijsen, E. M. 2010, A&A, 517, A77
- Vilardell, F., Ribas, I., Jordi, C., Fitzpatrick, E. L., & Guinan, E. F. 2010, A&A, 509, A70
- Weingartner, J. C., & Draine, B. T. 2001, ApJ, 548, 296
- Werner, M. W., Roellig, T. L., Low, F. J., et al. 2004, ApJS, 154, 1
- Xu, C., & Helou, G. 1996, ApJ, 456, 163
- Zurita, A., & Bresolin, F. 2012, MNRAS, 427, 1463